

See discussions, stats, and author profiles for this publication at: <https://www.researchgate.net/publication/230573707>

# Intramolecular Gas-Phase Reactions of Synthetic Nonheme Oxoiron(IV) Ions: Proximity and Spin-State Reactivity Rules

ARTICLE *in* CHEMISTRY - A EUROPEAN JOURNAL · SEPTEMBER 2012

Impact Factor: 5.73 · DOI: 10.1002/chem.201200105 · Source: PubMed

CITATIONS

3

READS

37

8 AUTHORS, INCLUDING:



**Rubén Mas-Ballesté**

Universidad Autónoma de Madrid

68 PUBLICATIONS 1,437 CITATIONS

SEE PROFILE



**Usharani Dandamudi**

Central Food Technological Research Instit...

27 PUBLICATIONS 314 CITATIONS

SEE PROFILE



**Sason Shaik**

Hebrew University of Jerusalem

527 PUBLICATIONS 20,677 CITATIONS

SEE PROFILE



**Lawrence Que**

University of Minnesota Twin Cities

451 PUBLICATIONS 25,894 CITATIONS

SEE PROFILE

# Intramolecular Gas-Phase Reactions of Synthetic Nonheme Oxoiron(IV) Ions: Proximity and Spin-State Reactivity Rules

Rubén Mas-Ballesté,<sup>[a, b]</sup> Aidan R. McDonald,<sup>[a]</sup> Dana Reed,<sup>[a]</sup> Dandamudi Usharani,<sup>[c]</sup> Patric Schyman,<sup>[c]</sup> Petr Milko,<sup>[c]</sup> Sason Shaik,<sup>\*,[c]</sup> and Lawrence Que, Jr.<sup>\*,[a]</sup>

**Abstract:** The intramolecular gas-phase reactivity of four oxoiron(IV) complexes supported by tetradentate N<sub>4</sub> ligands (**L**) has been studied by means of tandem mass spectrometry measurements in which the gas-phase ions [Fe<sup>IV</sup>(O)(**L**)(OTf)]<sup>+</sup> (OTf = trifluoromethanesulfonate) and [Fe<sup>IV</sup>(O)(**L**)]<sup>2+</sup> were isolated and then allowed to fragment by collision-induced decay (CID). CID fragmentation of cations derived from oxoiron(IV) complexes of 1,4,8,11-tetramethyl-1,4,8,11-tetraazacyclotetradecane (tmc) and *N,N'*-bis(2-pyridylmethyl)-1,5-diazacyclooctane (**L**<sup>8</sup>Py<sub>2</sub>) afforded the same predominant products irrespective of whether they were hexacoordinate or pentacoordinate. These products resulted from the loss of water by dehydrogenation of ethylene or propylene linkers on the

tetradentate ligand. In contrast, CID fragmentation of ions derived from oxoiron(IV) complexes of linear tetradentate ligands *N,N'*-bis(2-pyridylmethyl)-1,2-diaminoethane (bpmen) and *N,N'*-bis(2-pyridylmethyl)-1,3-diaminopropane (bpmpn) showed predominant oxidative N-dealkylation for the hexacoordinate [Fe<sup>IV</sup>(O)(**L**)(OTf)]<sup>+</sup> cations and predominant dehydrogenation of the diaminoethane/propane backbone for the pentacoordinate [Fe<sup>IV</sup>(O)(**L**)]<sup>2+</sup> cations. DFT calculations on [Fe<sup>IV</sup>(O)(bpmen)] ions showed that the experimentally observed preference for oxi-

dative N-dealkylation versus dehydrogenation of the diaminoethane linker for the hexa- and pentacoordinate ions, respectively, is dictated by the proximity of the target C–H bond to the oxoiron(IV) moiety and the reactive spin state. Therefore, there must be a difference in ligand topology between the two ions. More importantly, despite the constraints on the geometries of the TS that prohibit the usual upright  $\sigma$  trajectory and prevent optimal  $\sigma_{CH}-\sigma_{z^2}^*$  overlap, all the reactions still proceed preferentially on the quintet (*S*=2) state surface, which increases the number of exchange interactions in the d block of iron and leads thereby to exchange enhanced reactivity (EER). As such, EER is responsible for the dominance of the *S*=2 reactions for both hexa- and pentacoordinate complexes.

**Keywords:** bioinorganic chemistry • density functional calculations • exchange enhanced reactivity • hydrogen transfer • oxoiron complexes

## Introduction

Dioxygen-activating heme and nonheme iron enzymes participate in many oxidative transformations that are key to

the metabolism of living beings. Frequently oxoiron(IV) species are hypothesized to be the active oxidant in the catalytic cycles of these enzymes. For heme enzymes such as cytochrome P450, oxoiron(IV)–porphyrin  $\pi$ -cation radicals were found to be the active oxidant.<sup>[1]</sup> For nonheme iron enzymes<sup>[2]</sup> such as the  $\alpha$ -ketoglutarate ( $\alpha$ -KG)-dependent dioxygenases and pterin-dependent hydroxylases, the active oxidant was found to be an oxoiron(IV) species.<sup>[3]</sup> Mononuclear nonheme iron enzymes have been found to catalyze an array of oxidative conversions such as hydroxylation, halogenation, *cis*-dihydroxylation, desaturation, and N-dealkylation.<sup>[2a,b]</sup> Of particular interest to the present study are the  $\alpha$ -KG-dependent enzymes clavaminase synthase (CAS), which carries out desaturation reactions, and the alkylated DNA repair enzyme *AlkB*, which catalyzes oxidative N-demethylation. The oxoiron(IV) moiety that performs all of these transformations possesses the same intrinsic properties in all of these enzymes,<sup>[3d]</sup> with the active-site environment determining the outcome of the oxidative transformation (i.e., hydroxylation versus desaturation).<sup>[4]</sup> In the synthetic models, however, it is also possible to identify intrinsic factors that control the nature of the transformation.

[a] Dr. R. Mas-Ballesté, Dr. A. R. McDonald, Dr. D. Reed, Prof. L. Que, Jr.  
Department of Chemistry and  
Center for Metals in Biocatalysis  
University of Minnesota  
Minneapolis, MN 55455 (USA)  
E-mail: larryque@umn.edu

[b] Dr. R. Mas-Ballesté  
Departamento de Química Inorgánica  
Facultad de Ciencias, Universidad Autónoma de Madrid  
Ctra. de Colmenar Viejo Km 15, 28049 Madrid (Spain)

[c] Dr. D. Usharani, Dr. P. Schyman, Dr. P. Milko, Prof. S. Shaik  
Institute of Chemistry and the Lise Meitner-Minerva Center  
for Computational Quantum Chemistry  
The Hebrew University of Jerusalem  
91904 Jerusalem (Israel)  
E-mail: sason@yfaat.ch.huji.ac.il

Supporting information for this article is available on the WWW under <http://dx.doi.org/10.1002/chem.201200105>. It includes mass spectrometry data, computational details, geometrical parameters, energies, and xyz coordinates of all structures.

Recent results obtained with synthetic biomimetic oxoiron(IV) complexes have established high-valent nonheme oxoiron species as oxidants that are capable of an array of oxidative transformations.<sup>[5]</sup> These studies have also contributed to the understanding of the mechanistic landscape in the activation of dioxygen by nonheme iron enzymes. Important insights into the synthesis and characterization of a wide range of synthetic  $S=1$ <sup>[6]</sup> and  $S=2$ <sup>[7]</sup> oxoiron(IV) compounds have been reported. However, understanding the factors that regulate the reactivity of oxoiron(IV) species and the determination of selection rules for how the oxoiron(IV) unit interacts with substrate C–H bonds still remain as challenges. Of particular interest is the determination of which factors govern whether hydroxylation or dehydrogenation of an aliphatic substrate will occur. In this report, we present results from a study of four oxoiron(IV) complexes by using the electrospray ionization tandem mass spectrometry (ESI-MS-MS) technique to determine the collision-induced dissociation (CID) decay behavior of isolated oxoiron(IV) species in the gas phase. Our findings using the ESI-MS-MS technique, which are supported by DFT calculations, have unveiled new aspects of the oxoiron(IV) reaction landscape. The interplay of theory and experiment provides additional evidence for the involvement of the quintet state in intramolecular C–H bond cleavage even for situations where the Fe=O...HC angle deviates significantly from the ideal 180°.

## Experimental and Computational Methods

**Materials and methods:** All reagents were purchased from Aldrich and used as received unless noted otherwise. Iron(II) precursors were synthesized by procedures reported elsewhere.<sup>[8]</sup> CH<sub>3</sub>CN solvent was distilled over CaH<sub>2</sub> before use. Electronic absorption spectra were recorded using a Hewlett-Packard (Agilent) 8452 diode array spectrophotometer over a 190–1100 nm range in quartz cuvettes cooled to the desired temperature in a Unisoku cryostat.

Electrospray ionization mass spectral experiments were carried out using a Bruker BioTOF II mass spectrometer, whereas MS-MS analysis was carried out using a Bruker microTOF-Q instrument under the following conditions: spray chamber voltage 4000 V, drying gas temperature 200 °C. Quick injection of the sample into the spectrometer was carried out with a precooled syringe. Isolation of the observed cations was achieved by means of a quadrupole, and then their modes of decay were monitored in the collision cell of a quadrupole-TOF mass spectrometer. In these experiments, helium was used as the collision gas, and the degree of fragmentation was controlled by varying the potential used to accelerate the isolated ions. The use of argon or nitrogen gas produced significant fragmentation even at the lowest collision energies, but the use of helium allowed the observation of the behavior at the onset of fragmentation and was thus preferred. Because the CID experiments were carried out using a quadrupole-TOF mass spectrometer, the fragmentation conditions were necessarily multiple-collision. As such, the energies imparted to the ions under investigation are higher than the ion kinetic energy reported by the instrument software. However, the precise energy imparted to the ion is not well defined and cannot be used for quantitative dissociation energy measurements.

**Formation of oxoiron(IV) species:** The oxoiron(IV) complexes [Fe<sup>IV</sup>(O)-(tmc)(NCCH<sub>3</sub>)]<sup>2+</sup> and [Fe<sup>IV</sup>(O)(L<sup>8</sup>Py<sub>2</sub>)(NCCH<sub>3</sub>)]<sup>2+</sup> were prepared as previously described.<sup>[6a]</sup> Compound [Fe<sup>IV</sup>(O)(bpmpn)(NCCH<sub>3</sub>)]<sup>2+</sup> (**1**) was obtained by reacting 1 mM solutions of [Fe(bpmpn)(OTf)<sub>2</sub>] (2.0 mL;

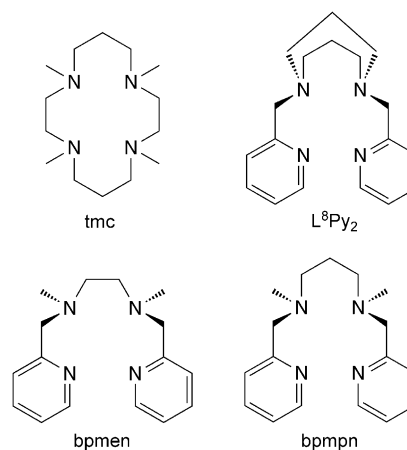
OTf = trifluoromethanesulfonate) in CH<sub>3</sub>CN in a 1 cm UV-visible cuvette precooled to –40 °C with 0.7 M CH<sub>3</sub>CO<sub>3</sub>H (28 μL, 10 equiv), and the reaction was followed by UV/Vis measurements. Maximal formation of **1** was achieved after approximately 20 min. The same procedure was followed to obtain compound [Fe<sup>IV</sup>(O)(bpmpn)(NCCH<sub>3</sub>)]<sup>2+</sup> (**2**) from [Fe<sup>II</sup>(bpmpn)(OTf)<sub>2</sub>], except that the reaction was carried out at 0 °C.

**DFT study:** All structures were optimized using spin-unrestricted B3LYP functionals and the LACVP(Fe)/6-31G(the rest) basis set, henceforth referred to as UB3LYP/B1.<sup>[9]</sup> The calculations were done with the Jaguar 7.6 program package.<sup>[10]</sup> Energy scans were conducted along an appropriate internuclear coordinate while optimizing freely the positions of all other atoms. The geometry at the top of the energy scan was used for subsequent optimization of a transition state. The transition states and minima were verified by frequency calculations at the UB3LYP/B1 level. Energy correction was done using a single-point calculation with a larger basis set B2, LACVP3P+(Fe)/6-311+G\*(the rest), hence, UB3LYP/B2//B1. Natural orbitals were calculated using Gaussian 03<sup>[11]</sup> based on the Jaguar guess wave function, and were drawn using Molekel.<sup>[12]</sup>

Initially, we optimized all the possible isomers (*cis-α*, *cis-β*, *cis-β'*, and *trans*, in *syn* or *anti* configuration) of the pentacoordinate [Fe<sup>IV</sup>(O)-(bpmpn)]<sup>2+</sup> and hexacoordinate [Fe<sup>IV</sup>(O)(bpmpn)(OTf)]<sup>+</sup> oxoiron complexes, in the  $S=1$  and  $S=2$  spin states, labeled as <sup>3,5</sup>K<sub>5</sub> and <sup>3,5</sup>K<sub>6</sub>. The pentacoordinate complexes were generated by removal of the OTf ligand and upon geometry optimization they all converged to distorted square-pyramidal geometries. The relative stabilities of the K<sub>5</sub> isomers were checked, adding empirical dispersion corrections, hence UB3LYP-D/B2//B1.<sup>[13]</sup> For the most stable K<sub>6</sub> isomer, we ascertained the relative spin-state ordering energies by using B3LYP\*, which contains 15 % exact exchange instead of the 20 % in B3LYP.<sup>[14]</sup> On the basis of the results, we selected the most stable <sup>3,5</sup>K<sub>6</sub> isomer and three of the appropriate <sup>3,5</sup>K<sub>5</sub> isomers for subsequent calculations of the regiochemical pathways described below. In addition, we investigated the decay mechanisms for [Fe<sup>IV</sup>(O)(L<sup>8</sup>Py<sub>2</sub>)]<sup>2+</sup>, [Fe<sup>IV</sup>(O)(tmc)]<sup>2+</sup>, and [Fe<sup>IV</sup>(O)(tmc)(OTf)]<sup>+</sup>, complexes for which the ligand topologies are fixed, as references for the *trans-syn-down* topology. All geometrical parameters (Figure S2–S15) and relative energies of key stationary points of reaction profiles (Tables S1–S18) are given in the Supporting information. Key results are presented in the paper.

## Results

**Oxoiron(IV) generation and characterization:** In this study, we have investigated four [Fe<sup>IV</sup>(O)(L)(NCCH<sub>3</sub>)]<sup>2+</sup> complexes supported by tetradentate N<sub>4</sub> ligands that adopt different ligand topologies around the oxoiron(IV) centers, in which L = tmc, L<sup>8</sup>Py<sub>2</sub>, bpmpn, and bpmpn (depicted below). The complexes of the first two ligands have been character-



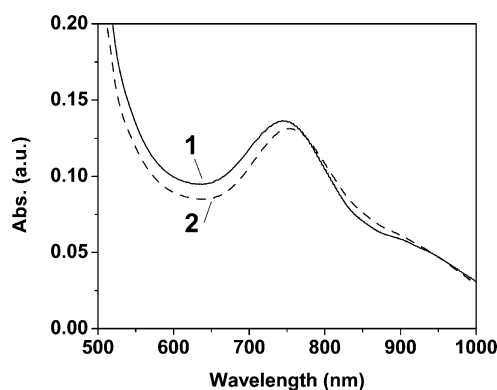


Figure 1. Electronic absorption spectra of **1** (solid trace) and **2** (dashed trace) generated by treating  $[\text{Fe}^{\text{II}}(\text{L})(\text{OTf})_2]$  (1 mM in  $\text{CH}_3\text{CN}$ ; **L** = bpmen, bpmnpn) with 10 equiv peracetic acid at  $-40$  and  $0^\circ\text{C}$ , respectively.

ized in detail in previous reports,<sup>[6a,g]</sup> whereas those of the latter two are more recent additions to the growing family of nonheme oxoiron(IV) complexes and are not as well characterized. We found that a tenfold excess amount of peracetic acid was required to obtain  $[\text{Fe}^{\text{IV}}(\text{O})(\text{bpmen})(\text{NCCH}_3)]^{2+}$  (**1**) and  $[\text{Fe}^{\text{IV}}(\text{O})(\text{bpmnpn})(\text{NCCH}_3)]^{2+}$  (**2**) in moderate yields (Figure 1). The formation of these oxoiron(IV) complexes was evidenced by the appearance of near-IR bands in their electronic absorption spectra ( $\lambda_{\text{max}} = 740$  nm for **1** and  $750$  nm for **2**; Figure 1). Evidence for the formation of **1** has been previously reported by Talsi and co-workers, who demonstrated that the reaction between  $[\text{Fe}^{\text{II}}(\text{bpmen})(\text{OTf})_2]$  and  $\text{H}_2\text{O}_2$  in the presence of acetic acid at  $-50^\circ\text{C}$  yielded **1** in approximately 30% yield,<sup>[15]</sup> and by Rybak-Akimova et al., who showed that the reaction of  $[\text{Fe}^{\text{II}}(\text{bpmen})(\text{OTf})_2]$  with the isopropyl ester of 2-iodoxybenzoic acid generated **1** in approximately 70% yield.<sup>[16]</sup> When compared with other  $S=1$  oxoiron(IV) complexes, **1** and **2** exhibit near-IR absorption maxima that fall between those of  $[\text{Fe}^{\text{IV}}(\text{O})(\text{tmc})(\text{NCCH}_3)]^{2+}$  (820 nm, no pyridine donors) and  $[\text{Fe}^{\text{IV}}(\text{O})(\text{N}_4\text{Py})]^{2+}$  (695 nm, four pyridine donors,  $\text{N}_4\text{Py} = N,N$ -bis(2-pyridylmethyl)- $N$ -bis(2-pyridyl)-methylamine). A molar extinction coefficient of about  $300 \text{ M}^{-1} \text{ cm}^{-1}$  was previously reported for oxoiron(IV) complexes with mixed amine/pyridine donors such as  $[\text{Fe}^{\text{IV}}(\text{O})(\text{TPA})(\text{NCCH}_3)]^{2+}$  ( $\lambda_{\text{max}} = 724$  nm;  $\epsilon = 300 \text{ M}^{-1} \text{ cm}^{-1}$ )<sup>[6b]</sup> and  $[\text{Fe}^{\text{IV}}(\text{O})(\text{L}^8\text{Py}_2)(\text{NCCH}_3)]^{2+}$  ( $\lambda_{\text{max}} = 790$  nm;  $\epsilon = 260 \text{ M}^{-1} \text{ cm}^{-1}$ )<sup>[6g]</sup>. With this in mind, we estimate maximum yields of around 50% for **1** and **2** when prepared with peracetic acid as oxidant at  $-40$  and  $0^\circ\text{C}$ , respectively.

The formulation of **1** and **2** as oxoiron(IV) complexes were further supported by their electrospray ionization mass spectra (ESI-MS). Dominant mass peaks were observed at  $m/z$  491.1 (for **1**) and  $m/z$  505.1 (for **2**) with mass values and isotope distribution patterns consistent with monocationic hexacoordinate  $[\text{Fe}^{\text{IV}}(\text{O})(\text{L})(\text{OTf})]^+$  ions (see Figure 2 for bpmen spectra). Mass peaks were also observed at  $m/z$  171.1 for **1** and  $m/z$  178.1 for **2**, which were

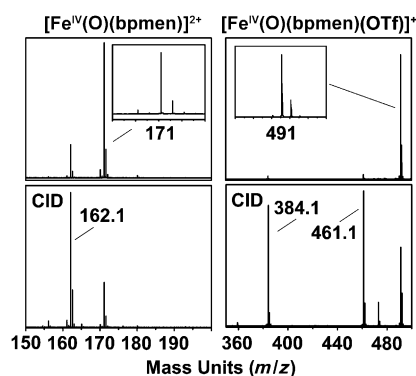


Figure 2. Top: ESI-MS spectra of the  $[\text{Fe}^{\text{IV}}(\text{O})(\text{bpmen})]^{2+}$  and  $[\text{Fe}^{\text{IV}}(\text{O})(\text{bpmen})(\text{OTf})]^+$  cations. Bottom: ESI-MS-MS results obtained in the CID decay of the isolated cations (also see Figure S1A–H in the Supporting Information).

consistent with the dicationic pentacoordinate species  $[\text{Fe}^{\text{IV}}(\text{O})(\text{L})]^{2+}$  (Figure 2). The observation of these ions allowed us to utilize tandem mass spectrometry,<sup>[18,19]</sup> to investigate the intramolecular oxidative decay of the four oxoiron(IV) complexes in this study and gain further understanding of the inherent reactivity properties of the oxoiron(IV) moiety.

Novel insights into the reactivity properties of the four oxoiron(IV) complexes were obtained by monitoring the decay of these species in the gas phase (Table 1). Isolation of the observed hexacoordinate  $[\text{Fe}^{\text{IV}}(\text{O})(\text{L})(\text{OTf})]^+$  and pentacoordinate  $[\text{Fe}^{\text{IV}}(\text{O})(\text{L})]^{2+}$  cations by means of a quadrupole allowed us to monitor their modes of collision-induced dissociation (CID) decay in the collision cell of a quadrupole-TOF mass spectrometer. (A closely related experiment was reported recently by O'Hair and co-workers in which an oxoiron(IV) ion, putatively  $S=2$ , was observed by monitoring the CID decay of a ( $\mu$ -oxo)diiron(III) complex, and the intermolecular reactivity of the ion with alcohol substrates was investigated.<sup>[20]</sup>) In our experiments, helium was used as the collision gas, and the degree of fragmentation was controlled by varying the applied potential to

Table 1. ESI-MS-MS fragmentation patterns observed in the CID decay of  $[\text{Fe}^{\text{IV}}(\text{O})(\text{L})(\text{OTf})]^+$  and  $[\text{Fe}^{\text{IV}}(\text{O})(\text{L})]^{2+}$  cations.<sup>[a]</sup>

$[\text{M}]^{+/2+}$	$[\text{M}-18]^{+/2+}$	$[\text{M}-30]^{+/2+}$	$[\text{M}-107]^{+/2+}$
$[\text{Fe}^{\text{IV}}(\text{O})(\text{tmc})(\text{OTf})]^+$	✓ <sup>[b]</sup>	–	–
$[\text{Fe}^{\text{IV}}(\text{O})(\text{tmc})]^{2+}$	✓✓	–	–
$[\text{Fe}^{\text{IV}}(\text{O})(\text{L}^8\text{Py}_2)(\text{OTf})]^+$	✓✓ <sup>[c]</sup>	–	✓
$[\text{Fe}^{\text{IV}}(\text{O})(\text{L}^8\text{Py}_2)]^{2+}$	✓✓	–	–
$[\text{Fe}^{\text{IV}}(\text{O})(\text{bpmen})(\text{OTf})]^+$	–	✓✓	✓
$[\text{Fe}^{\text{IV}}(\text{O})(\text{bpmen})]^{2+}$	✓✓	–	–
$[\text{Fe}^{\text{IV}}(\text{O})(\text{bpmnpn})(\text{OTf})]^+$	–	✓	✓✓
$[\text{Fe}^{\text{IV}}(\text{O})(\text{bpmnpn})]^{2+}$	✓✓	✓	–

[a]  $[\text{M}]^{+/2+}$  corresponds to the mass fragment of interest.  $[\text{M}-18]^{+/2+}$  = loss of  $\text{H}_2\text{O}$ ;  $[\text{M}-30]^{+/2+}$  = loss of  $\text{CH}_2\text{O}$ ;  $[\text{M}-107]^{+/2+}$  = loss of  $\text{PyCHO}$ . ✓✓ represents the dominant peak in the CID spectra and ✓ represents a peak (not the dominant one) that is observed. [b] An  $[\text{M}-56]^+$  peak was also observed, which corresponds to the loss of a  $\text{C}_3\text{H}_4\text{O}$  fragment that must derive from initial hydrogen-atom abstraction from the propylene linker. This peak is in fact more intense than the  $[\text{M}-18]^+$  peak. [c] An  $[\text{M}-150]^+$  peak is also observed that corresponds to loss of  $\text{CF}_3\text{SO}_3\text{H}$  instead of  $\text{H}_2\text{O}$ .

accelerate the isolated ions. Helium was chosen for these experiments due to its low mass, as other gases such as argon and nitrogen produced significant fragmentation of these ions even at retarding potentials. Fragmentation of the isolated hexacoordinate  $[\text{Fe}^{\text{IV}}(\text{O})(\text{L}^8\text{Py}_2)(\text{OTf})]^+$  monocation afforded  $[M-18]^+$  (loss of  $\text{H}_2\text{O}$ ) and  $[M-107]^+$  (loss of  $\text{PyCHO}$ ) products, whereas decay of the pentacoordinate  $[\text{Fe}^{\text{IV}}(\text{O})(\text{L}^8\text{Py}_2)]^{2+}$  dication gave rise only to the loss of water (Figure S1A–H in the Supporting Information). As the  $\text{L}^8\text{Py}_2$  ligand contains propylene and  $\text{Py-CH}_2$  groups bound to tertiary amine moieties, the observed CID products would suggest that the oxoiron(IV) moiety decays primarily by dehydrogenation of the propylene chain (thereby resulting in loss of  $\text{H}_2\text{O}$  or  $\text{CF}_3\text{SO}_3\text{H}$ ) or oxidative N-dealkylation of the N- $\text{CH}_2$ -Py groups (Table 1). In contrast, for  $[\text{Fe}^{\text{IV}}(\text{O})(\text{tmc})(\text{OTf})]^+$  and  $[\text{Fe}^{\text{IV}}(\text{O})(\text{tmc})]^{2+}$ , which contain N- $\text{CH}_3$ , ethylene, and propylene groups, the decay product ions observed exclude attack of the N- $\text{CH}_3$  groups (Table 1). The absence of N-demethylation products ( $[M-30]^{+/2+}$ , N- $\text{CH}_3$  oxidation) can be rationalized by the crystal structure of  $[\text{Fe}^{\text{IV}}(\text{O})(\text{tmc})(\text{NCCH}_3)]^{2+}$ , in which the N- $\text{CH}_3$  groups are oriented *anti* with respect to the oxoiron(IV) moiety and thus too far away from the oxoiron(IV) unit to be susceptible to an intramolecular attack.<sup>[6a]</sup> The decay of  $[\text{Fe}^{\text{IV}}(\text{O})(\text{tmc})(\text{OTf})]^+$  yields  $[M-18]^+$  and  $[M-56]^+$  fragments. The latter corresponds to the loss of an oxygen atom and a three-carbon chain, strongly suggesting that it is the propylene linker that is attacked in the course of CID decay. These accumulated observations strongly suggest that the observed fragmentation patterns result from proximity of a susceptible C–H bond to the oxoiron(IV) unit.

In stark contrast, the fragmentation patterns of **1** and **2** depend on whether the precursor ion is the hexacoordinate monocation or the pentacoordinate dication. As depicted in Figure 2, the monocation of **1** decayed by the loss of either  $[M-30]^+$  or  $[M-107]^+$  mass unit fragments, which correspond either to the loss of  $\text{CH}_2\text{O}$  or  $\text{PyCHO}$ . On the other hand, the dication of **1** decayed by the loss of an 18 mass unit fragment, which was assigned to the loss of  $\text{H}_2\text{O}$  presumably as a result of the oxidative dehydrogenation of the ligand ethylene backbone. The data suggests that the oxoiron(IV) moiety in  $[\text{Fe}^{\text{IV}}(\text{O})(\text{bpmen})(\text{OTf})]^+$  reacted more readily with the N- $\text{CH}_3$  and N- $\text{CH}_2$ -Py hydrogen atoms to proceed along an oxidative N-dealkylation pathway, whereas  $[\text{Fe}^{\text{IV}}(\text{O})(\text{bpmen})]^{2+}$  preferably reacted with the hydrogen atoms of the ethylene bridge and instead underwent oxidative dehydrogenation in its decay. These observations would suggest that the oxoiron(IV) moiety in the hexacoordinate  $[\text{Fe}^{\text{IV}}(\text{O})(\text{bpmen})(\text{OTf})]^+$  ion interacts with the ligand framework in a different manner from that in the pentacoordinate  $[\text{Fe}^{\text{IV}}(\text{O})(\text{bpmen})]^{2+}$  ion. This outcome can be rationalized by considering that loss of the  $^-\text{OTf}$  ligand leads to a much greater degree of topological freedom for the pentacoordinate  $[\text{Fe}^{\text{IV}}(\text{O})(\text{bpmen})]^{2+}$  ion, hence opening up alternative avenues for decay. A similar decay pattern was observed for complex **2** with N-dealkylation for the coordina-

tively saturated  $[\text{Fe}^{\text{IV}}(\text{O})(\text{bpmpn})(\text{OTf})]^+$  ion versus dehydrogenation for the coordinatively unsaturated  $[\text{Fe}^{\text{IV}}(\text{O})(\text{bpmpn})]^{2+}$  ion (Figure S1C,D in the Supporting Information). However, the observed contrasting CID decay behavior cannot have a simple hexa- versus pentacoordinate rationale, as both dehydrogenation and N-dealkylation are observed for the hexacoordinate  $[\text{Fe}^{\text{IV}}(\text{O})(\text{L}^8\text{Py}_2)(\text{OTf})]^+$  ion and only dehydrogenation is found for the pentacoordinate  $[\text{Fe}^{\text{IV}}(\text{O})(\text{L}^8\text{Py}_2)]^{2+}$  ion.

What makes the  $\text{L}^8\text{Py}_2$  ligand different from the tetradentate ligands of **1** and **2** is the topological rigidity of  $\text{L}^8\text{Py}_2$ , due to the two propylene linkers that enforce a *trans* topology about the iron center.<sup>[6a]</sup> On the other hand, bpmen and bpmpn can in principle adopt a number of topologies. Depending on the topology adopted, different C–H bonds would come into closer proximity of the oxoiron(IV) unit, which could then abstract the hydrogen atom from that C–H bond, thereby leading to N-dealkylation or desaturation. It would thus appear that the selectivity for N-dealkylation versus dehydrogenation is related to the accessibility of the oxo moiety to the respective C–H bonds for hydrogen-atom abstraction. This selectivity will be referred to hereafter as “the proximity rule.” The intramolecular oxidative decay of oxoiron(IV) complexes is a very important discovery and demonstrates the potency of the oxoiron(IV) moiety even in intramolecular hydrogen-atom abstraction in which the  $\text{Fe=O}$  and C–H units are constrained to have relative orientations that are less than ideal for C–H bond cleavage. We have thus employed DFT analysis to determine whether the divergent reactivity pathways for the hexa- and pentacoordinate ions of **1** and **2** are indeed due to topological differences or whether there is any intrinsic factor for the observed selectivity.

#### DFT investigations of $[\text{Fe}^{\text{IV}}(\text{O})(\text{bpmen})(\text{OTf})]^+$ , $[\text{Fe}^{\text{IV}}(\text{O})(\text{bpmen})]^{2+}$ , $[\text{Fe}^{\text{IV}}(\text{O})(\text{L}^8\text{Py}_2)]^{2+}$ , $[\text{Fe}^{\text{IV}}(\text{O})(\text{tmc})(\text{OTf})]^+$ , and $[\text{Fe}^{\text{IV}}(\text{O})(\text{tmc})]^{2+}$

*bpmen-based isomers and spin states:* DFT calculations were performed on the hexa- and pentacoordinate ions of **1**, henceforth named **K**<sub>6</sub> and **K**<sub>5</sub>, respectively, to understand the distinct regiochemistries observed in intramolecular decay by the two complexes. To date, all solid-state structures of  $[\text{Fe}(\text{bpmen})]$  complexes show that the bpmen ligand adopts a *cis-α* topology about the iron center with the two N- $\text{CH}_3$  groups *anti* with respect to each other.<sup>[21]</sup> In contrast, the related bpmpn ligand can adopt different topologies in the few crystal structures of iron complexes that are available, including *cis-α-anti*, *cis-β-anti*, *cis-β-syn*, and *trans-syn* modes.<sup>[8b,21b,c]</sup> Under the right solvent conditions, facile interconversion among the different ligand topologies has been demonstrated for iron(II) complexes.

**K**<sub>6</sub> and **K**<sub>5</sub> can exist potentially as nine distinct isomers defined by the relationship of the N- $\text{CH}_2$ -Py and N- $\text{CH}_3$  moieties, designated as having *cis-α*, *cis-β*, *cis-β'*, or *trans* topologies and with methyl groups in a *syn* (up or down) or *anti* configuration relative to each other. All of the **K**<sub>6</sub> isomers

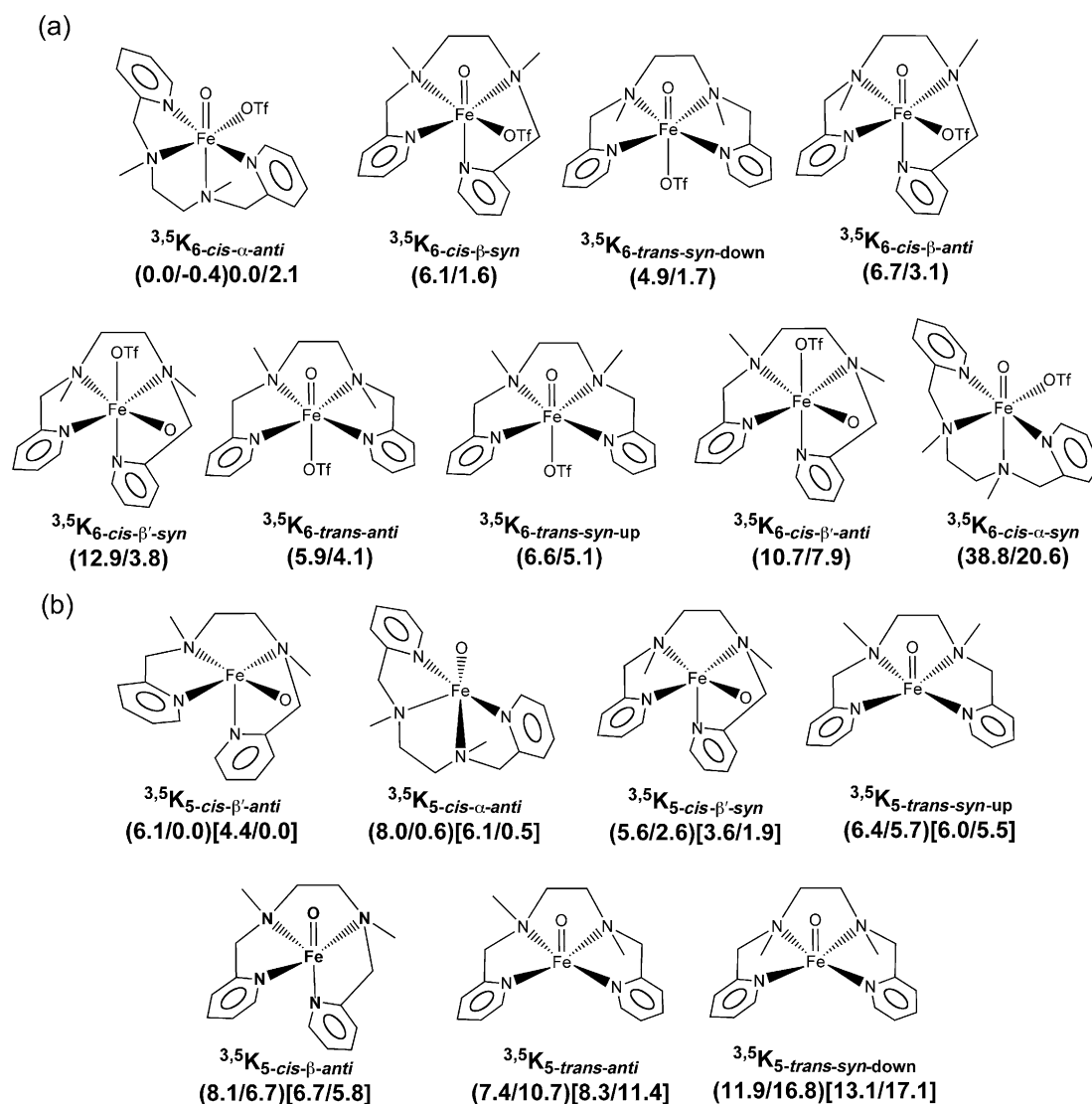


Figure 3. Schematic presentation of possible a) hexacoordinate  $[\text{Fe}^{\text{IV}}(\text{O})(\text{bpmen})(\text{OTf})]^+$  ( $\mathbf{K}_6$ ) and b) pentacoordinate  $[\text{Fe}^{\text{IV}}(\text{O})(\text{bpmen})]^{2+}$  ( $\mathbf{K}_5$ ) complexes. Beneath the structures, we show the relative free energies [ $\text{kcal mol}^{-1}$ ] for the  $S=1/S=2$  spin states. In each set the most stable isomer in the lowest spin state defines the zero of the relative energy scales. Values in parentheses are at the UB3LYP/B2//B1 level, values in square brackets pertain to UB3LYP-D/B2//B1 values. For  $^{3,5}\mathbf{K}_6$ -*cis- $\alpha$ -anti*, the two values not in parentheses correspond to UB3LYP\*/B2//B1 values.

were found to possess octahedral geometries, whereas loss of the  $^-\text{OTf}$  ligand leads to the  $\mathbf{K}_5$  isomers that assume distorted square-pyramidal geometries. These isomers and their calculated relative free energies are depicted in Figure 3. Two topologically flexible  $\mathbf{K}_5$  isomers, *cis- $\alpha$ -syn* and *cis- $\beta$ -syn*, are not shown, as they converged to the *cis- $\beta'$ -syn* isomer on both spin-state surfaces (for detailed geometric parameters see Figure S2 in the Supporting Information).

Inspection of Figure 3a shows that the most stable  $\mathbf{K}_6$  isomer is the *cis- $\alpha$ -anti* form. It mirrors the only topology found for the bpmen ligand in crystallographically characterized complexes.<sup>[21]</sup> At the UB3LYP/B1 level,  $\mathbf{K}_6$ -*cis- $\alpha$ -anti* has a triplet ( $S=1$ ) ground state (Figure S2A in the Supporting Information), whereas with B2 the  $S=1$  and  $S=2$  states are virtually degenerate. A single-point calculation at the UB3LYP\*/B2 level slightly favors  $S=1$ . In  $\mathbf{K}_6$ -*cis- $\alpha$ -anti*, the N- $\text{CH}_2$ -Py and N- $\text{CH}_3$  groups are in closer proximity to the

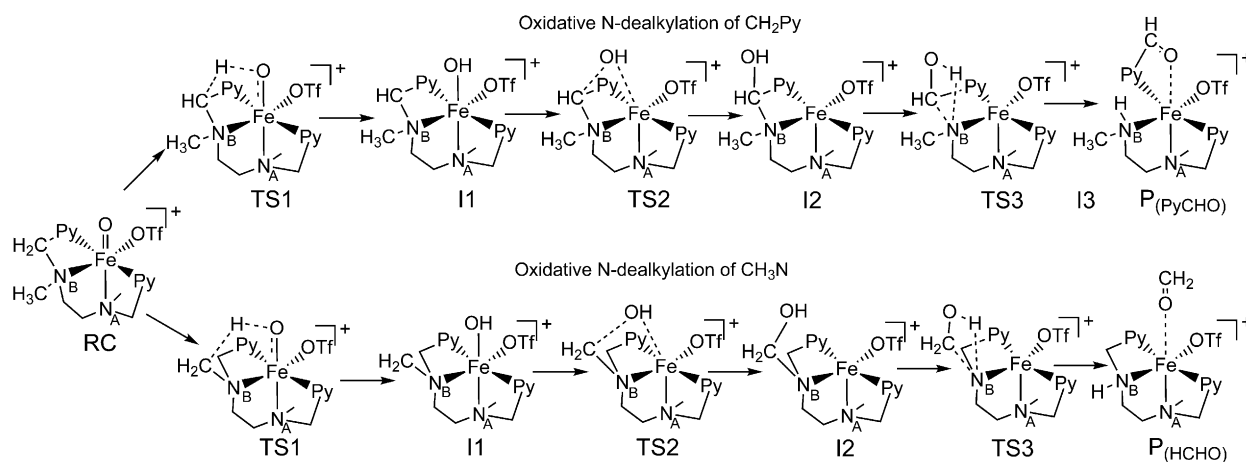
oxoiron(IV) moiety than the ethylene linker and would thus serve as the targets of the oxoiron(IV) unit for hydrogen-atom abstraction. We therefore selected this isomer for the extensive DFT studies into its reactivity.

Figure 3b shows the  $\mathbf{K}_5$  isomers and their relative energies. Here the most stable *cis- $\beta'$ -anti* isomer possesses a quintet ( $S=2$ ) ground state, but the others seem to prefer  $S=1$ . At the UB3LYP/B2 level, the most stable isomers are those that have *cis- $\beta$*  topology, whereas the *trans* isomers, which possess a strong equatorial ligand field and more strain in the diaminoethane linker, are higher in energy (Figure S2B in the Supporting Information). The UB3LYP-D//B2 result shows that the relative isomer stability is not affected by incorporation of dispersion, and we therefore conclude that the  $\mathbf{K}_5$ -*cis* isomers are the most stable ones. It must be noted that, according to the proximity rule, the *cis* isomers would not be predisposed to oxidation of the 1,2-diaminoethane

linker, which is far from the oxoiron(IV) moiety, and will possess very high-energy TS. However, they can undergo interconversion to *trans* isomers, which would bring the linker close to the oxoiron(IV) center and allow its oxidation by initial hydrogen abstraction. These interconversions are relatively facile Berry-type processes with free energy (UB3LYP/B2) barriers of 7.0/8.4 kcal mol<sup>-1</sup> (*S*=1/*S*=2) for *cis*- $\alpha$ -*anti* to *cis*- $\beta$ -*anti*, and 5.1/5.7 kcal mol<sup>-1</sup> (*S*=1/*S*=2) for *cis*- $\beta$ -*anti* to *trans*-*anti* (UB3LYP/B2; Scheme S1 in the Supporting Information). As such, we have proceeded to investigate the reactivity of **K**<sub>5-*trans*-*anti*</sub> that has all three different groups in proximity to the Fe=O moiety (Figure 3b). We could not find any low-energy isomerization pathway that

leads to the **K**<sub>5-*trans*-*syn*-*down*</sub> isomer; nevertheless, we have found it necessary to investigate the reactivity of this isomer as well, for reasons to be made clear later.

**Reaction mechanism for the **K**<sub>6-*cis*- $\alpha$ -*anti*</sub> isomer of [Fe<sup>IV</sup>(O)-(bpmen)(OTf)]<sup>+</sup>:** In the hexacoordinate *cis*- $\alpha$ -*anti* isomer, the hydrogen atoms in the N-CH<sub>3</sub> and N-CH<sub>2</sub>-Py moieties of the bpmen ligand are in close proximity to the oxoiron(IV) moiety. The N-dealkylation process generally involves three steps:<sup>[22]</sup> Hydrogen-atom abstraction, rebound, and carbinol decomposition, as depicted in Scheme 1 for the N-dealkylation processes nascent from **K**<sub>6-*cis*- $\alpha$ -*anti*</sub>.



Scheme 1. Schematic representation of intramolecular oxidative N-dealkylation in **K**<sub>6-*cis*- $\alpha$ -*anti*</sub> (Py=pyridine ring).

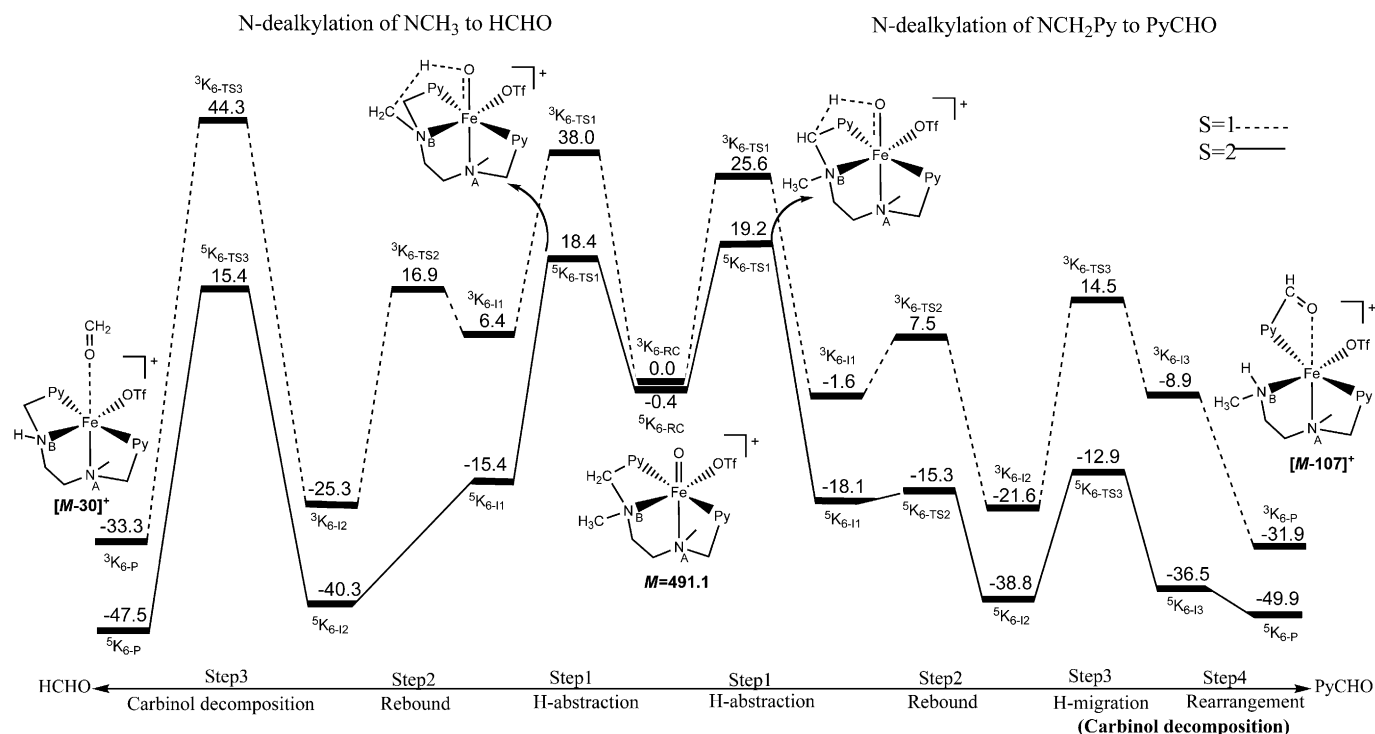


Figure 4. Free-energy profiles [kcal mol<sup>-1</sup>] at the B2//B1 level for the reactions of the hexacoordinate complex [Fe<sup>IV</sup>(O)(bpmen)(OTf)]<sup>+</sup> (<sup>3,5</sup>**K**<sub>6-*cis*- $\alpha$ -*anti*</sub>). The reactant state is in the middle of the diagram, and going to the left describes the profile for the N-CH<sub>3</sub> dealkylation, whereas to the right is the N-CH<sub>2</sub>-Py dealkylation. The reference 0.0 energy is the <sup>3</sup>**K**<sub>6-*cis*- $\alpha$ -*anti*</sub> reactant state in the midpoint of the diagram.

Figure 4 shows the energy profiles for these processes starting from the  $S=1$  and  $S=2$  states of  $^{3,5}\mathbf{K}_{6\text{-cis-}\alpha\text{-anti}}$ . It is apparent that the quintet state has a clear advantage as observed in all previous investigations into nonheme oxoiron(IV) reactions. This advantage is caused by exchange-enhanced reactivity (EER), due to the increase in the number of unpaired d electrons in the hydrogen-abstraction transition states.<sup>[4e,23]</sup>

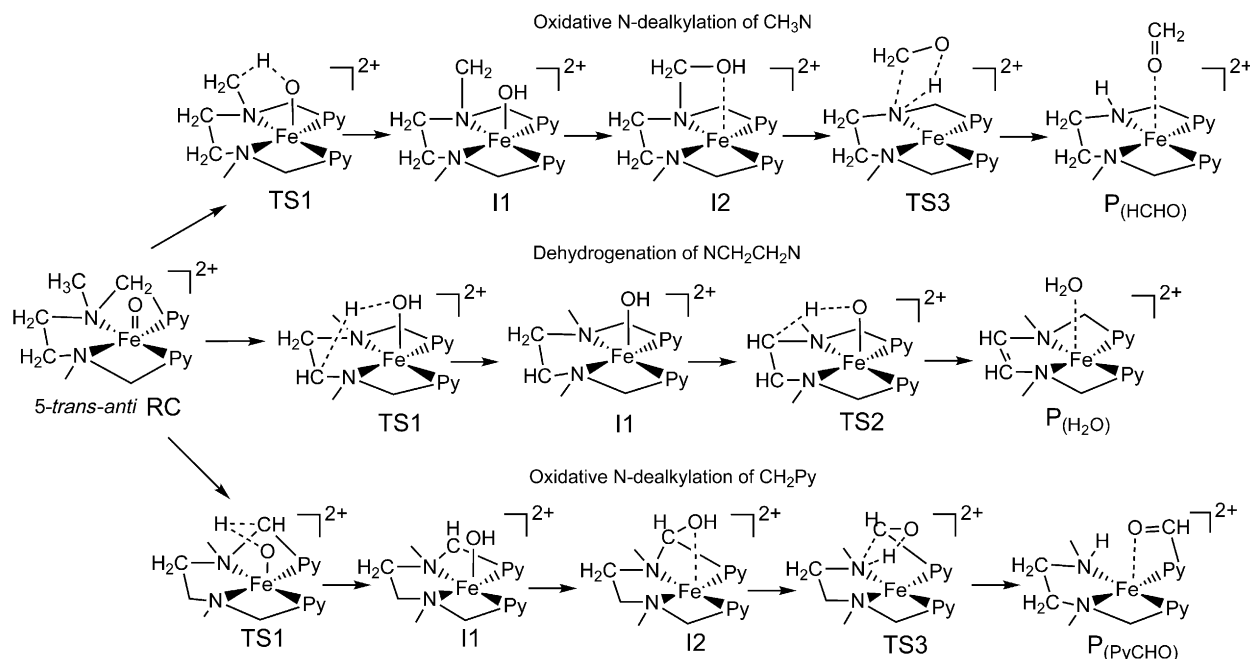
In discussing the observed regioselection in the CID experiment, we must recall that this is a gas-phase reaction, in which the excess energy does not dissipate, and hence the reaction complex conserves the initial energy of  $^{3,5}\mathbf{K}_6$ , and the resulting intermediates past the first hydrogen-abstraction events do not equilibrate in the deeper energy wells. Furthermore, upon collision, part of the kinetic energy of the ions is converted to internal energy that induces the intramolecular reactivity observed in the CID experiment. In this sense, inspection of Figure 4 shows that the rate-determining step for both dealkylation processes is the first hydrogen-atom abstraction, with very close free-energy barriers on the  $S=2$  profiles (18.4 and 19.2 kcal mol<sup>-1</sup> for attack of N-CH<sub>3</sub> and N-CH<sub>2</sub>-Py groups, respectively); the rest of the barriers (relative to the reactant onset) are smaller and will not affect the regioselectivity. This is in accord with experimental results, which exhibit both  $[M-30]^+$  and  $[M-107]^+$  peaks with higher intensity for the  $[M-30]^+$  peak (Table 1, Figure 2). Note also that the  $S=1$  barriers are high and the 12 kcal mol<sup>-1</sup> higher barrier for methyl attack predicts the observation of only the  $[M-107]^+$  peak, in discord with the experimental findings in Table 1. Therefore, the match of the  $S=2$  barriers to the CID experiment gives experimental support for  $S=2$  reactivity. We also point out that, unlike the earlier reports on the intermolecular reactions of tertiary amines with heme and nonheme oxidants in

solution and the gas phase,<sup>[24]</sup> there is no initial electron transfer from the amine moiety to the Fe<sup>IV</sup> center, because the amine lone pairs in  $^{3,5}\mathbf{K}_{6\text{-cis-}\alpha\text{-anti}}$  are coordinated to the metal center.

**Reaction mechanisms for the  $\mathbf{K}_{5\text{-trans-anti}}$  and  $\mathbf{K}_{5\text{-trans-syn}}$  isomers of  $[\text{Fe}^{\text{IV}}(\text{O})(\text{bpmen})]^{2+}$ :** Scheme 2 describes the steps in the mechanisms of the various reactions that the *trans* isomers may undergo in the CID experiment. By analogy to previous studies,<sup>[4e,25,26]</sup> the dehydrogenation path can involve two consecutive hydrogen-atom abstractions, first by oxoiron(IV) and then followed by the reduced hydroxoiron(III) product.

**Reactivity of the  $^{3,5}\mathbf{K}_{5\text{-trans}}$  isomers:** For all the *trans* isomers, the hydrogen atoms of the N-(CH<sub>2</sub>)<sub>2</sub>-N, the N-CH<sub>2</sub>-Py, and sometimes also the N-CH<sub>3</sub> moieties are in close proximity to the oxoiron(IV) moiety, and may therefore lead to dehydrogenation and oxidative N-dealkylation products. We have therefore screened the decay behavior of five different pentacoordinate isomers. Two of these are the stable *cis* isomers *cis- $\alpha$ -anti* and *cis- $\beta'$ -anti*, which as already stated converted during the hydrogen abstraction by a facile Berry process to the *trans-anti* isomer. We therefore ended up screening the *trans-anti*, *trans-syn-up*, and *trans-syn-down* isomers. It should be noted that, despite the differences among these three *trans* isomers, all of them have clearly lower free-energy barriers on the  $S=2$  surface (Figure 5a and b, as well as Figures S3 and S4 in the Supporting Information).

Figure 5a shows the free-energy profiles of N-(CH<sub>2</sub>)<sub>2</sub>-N desaturation and N-CH<sub>3</sub> dealkylation reactions for  $^{3,5}\mathbf{K}_{5\text{-trans-anti}}$ . It is seen that, even though the triplet state is lower in energy by 3.3 kcal mol<sup>-1</sup> than the quintet state, the



Scheme 2. Schematic representation of intramolecular decay pathways in the pentacoordinate complex  $[\text{Fe}^{\text{IV}}(\text{O})(\text{bpmen})]^{2+}$ .



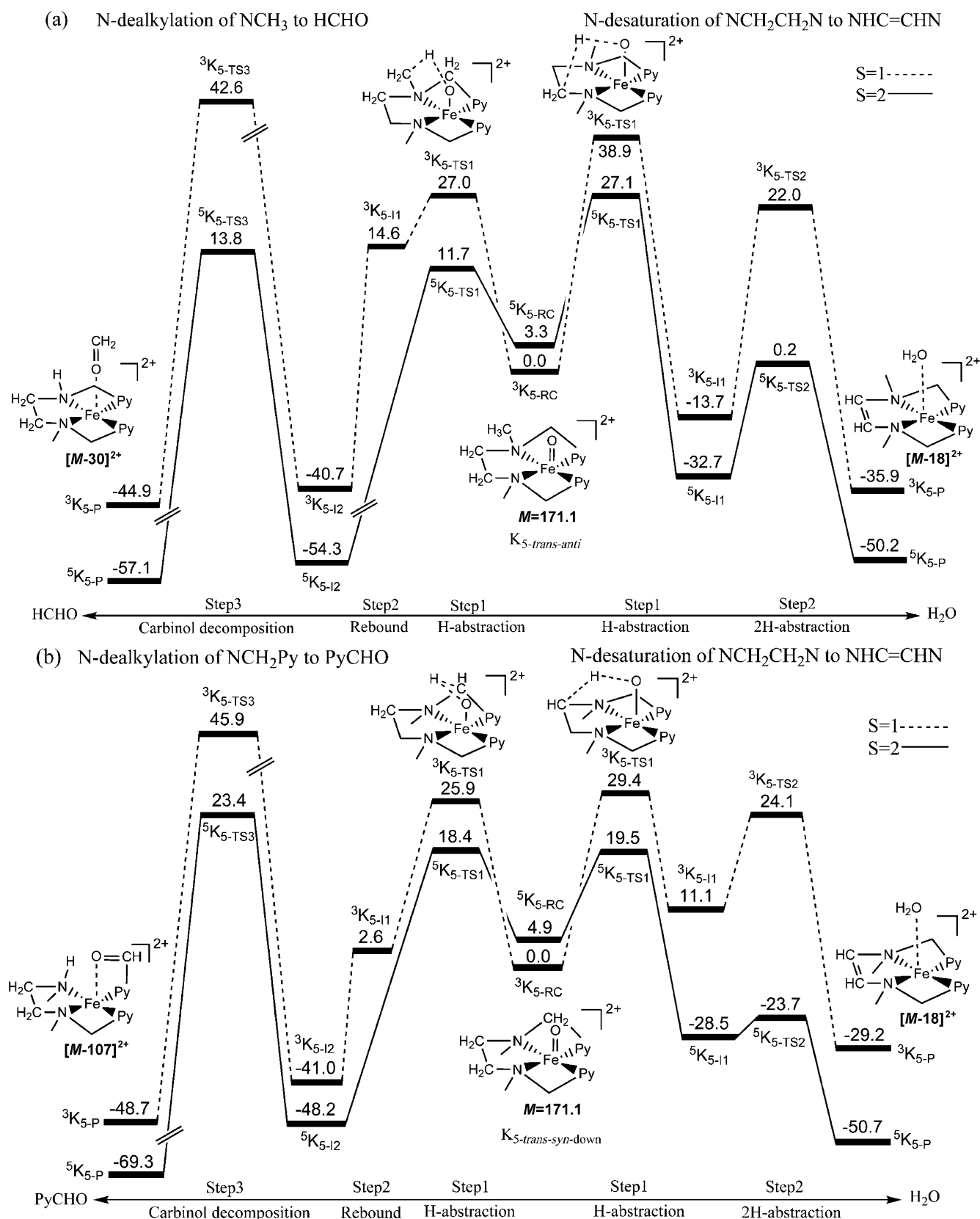


Figure 5. Free-energy profiles [kcal mol<sup>-1</sup>] at the B2//B1 level of theory for the reactions of the pentacoordinate [Fe<sup>IV</sup>(O)(bpmen)]<sup>2+</sup> complexes: a) <sup>3,5</sup>K<sub>5</sub>-trans-anti and b) <sup>3,5</sup>K<sub>5</sub>-trans-syn-down. In each case, the reactant state is in the middle of the diagram, and going to the left describes the profile for the respective N-dealkylation steps, whereas to the right is the dehydrogenation of the N-(CH<sub>2</sub>)<sub>2</sub>-N linker. The reference 0.0 energy is the <sup>3</sup>K<sub>5</sub>-RC reactant state in the midpoint of the figure.

oxoiron(IV) reaction landscape is still dominated by the quintet  $S=2$  state, thus revealing the importance of the EER effect once again.<sup>[23g,h]</sup> If we start with an assumption that the internal energy imparted to the pentacoordinate complex during the collision with He is not sufficient to cross the high barriers on the  $S=1$  surface, then we must rely only on the barriers of the  $S=2$  surface. Thus, as shown in Figure 5a, the first hydrogen-atom abstraction steps (through  $^5\mathbf{K}_{5\text{-TS1}}$ ) from N-(CH<sub>2</sub>)<sub>2</sub>-N and N-CH<sub>3</sub> have barriers of 27.1 and 11.7 kcal mol<sup>-1</sup>, respectively (the barrier for hydrogen abstraction from N-CH<sub>2</sub>-Py is 19.9 kcal mol<sup>-1</sup>; see Figure S3 in the Supporting Information). The subsequent barrier for CH<sub>2</sub>O elimination is 13.8 kcal mol<sup>-1</sup> relative to the reactant onset. The addition of dispersion correction changes these values by only 0.5–1.7 kcal mol<sup>-1</sup>, and hence the trends remain identical to those in Figure 5a. As such, following the rule of conservation of energy in gas-phase reactivity, Figure 5a predicts that on the  $S=2$  surface the  $[M-30]^{2+}$  ion will be the only observed peak in the CID, which is, however, inconsistent with experimental results (Table 1). Calculations on another *trans* isomer,  $^{3,5}\mathbf{K}_{5\text{-trans-syn-up}}$ , make an identical prediction, which is again incorrect (see Figure S4 in the Supporting Information). Note, however, that if sufficient energy were available to cross over to the  $S=1$  surface, the free-energy barriers in Figure 5a would predict a favored desaturation ( $[M-18]^{2+}$ ) for the  $^3\mathbf{K}_{5\text{-trans-anti}}$  isomer (but not for  $^3\mathbf{K}_{5\text{-trans-syn-up}}$ ; see Figure S4 in the Supporting Information), which would be in accord with the observed CID results.

To ascertain whether the larger barriers for the first hydrogen abstraction from N-(CH<sub>2</sub>)<sub>2</sub>-N in  $\mathbf{K}_{5\text{-trans-anti}}$  and  $^5\mathbf{K}_{5\text{-trans-syn-up}}$  originate from adverse effects of the up-pointing methyl group or not, we decided to examine  $^{3,5}\mathbf{K}_{5\text{-trans-syn-down}}$  as well, wherein the methyl group points downward and away from the hydrogen-abstraction trajectory. Thus, in this isomer the two proximal groups to the oxoiron(IV) moiety are N-CH<sub>2</sub>-Py and N-(CH<sub>2</sub>)<sub>2</sub>-N, and the results are shown in Figure 5b. It is seen that the rate-determining free-energy barriers on the  $S=2$  surface are now 19.5 kcal mol<sup>-1</sup> (through  $^5\mathbf{K}_{5\text{-TS1}}$ ) for hydrogen abstraction from the N-(CH<sub>2</sub>)<sub>2</sub>-N linker versus 23.4 (through  $^5\mathbf{K}_{5\text{-TS3}}$ ) for the elimination of the PyCHO moiety. Therefore, these calculations predict that this isomer, were it available, would lead mostly, if not only, to an  $[M-18]^{2+}$  peak. This computed preference for dehydrogenation is in accord with the presence of the  $[M-18]^{2+}$  mass peak and the absence of peaks that correspond to the loss of N-dealkylated products in the CID decay of  $[\text{Fe}^{\text{IV}}(\text{O})(\text{bpmen})]^{2+}$  (Figure 2). However, we could not find a low-energy mechanism for the generation of  $^5\mathbf{K}_{5\text{-trans-syn-down}}$  from the more stable pentacoordinate complexes. Nevertheless, it should be noted that the pentacoordinate complex has a dipositive charge and a somewhat lower mass than the hexacoordinate one (342 versus 491 amu), which will cause its acceleration energy at a given voltage to be at least twice as large as that of the monopositive hexacoordinate complex, so we cannot rule out the possibility that the  $[\text{Fe}^{\text{IV}}(\text{O})(\text{bpmen})]^{2+}$  complex acquires upon

collision with He sufficient internal energy to isomerize from the original topology.<sup>[27]</sup> Thus, if we accept the hypothesis that higher energy is available to the pentacoordinate  $[\text{Fe}^{\text{IV}}(\text{O})(\text{bpmen})]^{2+}$  complex in the CID experiment, then there are two scenarios that match the experimental observation. In the first one,  $\mathbf{K}_{5\text{-trans-anti}}$  is the reactive isomer, and the resultant  $[M-18]^{2+}$  peak in the CID spectrum corresponds to a triplet-state decay (Figure 5a). In the second scenario, the isomer  $\mathbf{K}_{5\text{-trans-syn-down}}$  is formed and its quintet state is responsible for the observed  $[M-18]^{2+}$  peak. Theory cannot distinguish between these two scenarios.

To test decay patterns with a structure analogous to the *trans-syn-down* isomer of bpmen, we further investigated  $[\text{Fe}^{\text{IV}}(\text{O})(\text{L}^8\text{Py}_2)]^{2+}$ ,  $[\text{Fe}^{\text{IV}}(\text{O})(\text{tmc})(\text{OTf})]^+$ , and  $[\text{Fe}^{\text{IV}}(\text{O})(\text{tmc})]^{2+}$ . The tmc complex was chosen in particular because it is crystallographically established to exist in the *trans-syn-down* topology.<sup>[6a]</sup> Although not crystallographically characterized, the  $\text{L}^8\text{Py}_2$  complex is constrained to adopt a similar topology. Indeed all three ions also exhibited a preponderant  $[M-18]^{2+}$  peak in the CID spectra (Table 1).

#### Reaction mechanism for $\mathbf{K}_{5\text{-trans}}$ isomer of $[\text{Fe}^{\text{IV}}(\text{O})(\text{L}^8\text{Py}_2)]^{2+}$ :

In the *trans* isomer, some of the hydrogen atoms of the N-(CH<sub>2</sub>)<sub>3</sub>-N and the N-CH<sub>2</sub>-Py moieties face the oxoiron(IV) moiety. The barriers for the first hydrogen abstraction are 32.9 ( $S=1$ )/23.5 ( $S=2$ ) for N-CH<sub>2</sub>-Py activation and 28.5 ( $S=1$ )/18.2 ( $S=2$ ) kcal mol<sup>-1</sup> N-(CH<sub>2</sub>)<sub>3</sub>-N (Figure S5 in the Supporting Information). Thus, in accord with the bpmen case, the reaction should prefer the quintet surface here too. However, unlike the bpmen complex, here the DFT calculations predict a preferable H<sub>2</sub>O loss over PyCHO, which is in accord with experiment (Table 1).

#### Reaction mechanism for the $\mathbf{K}_{5\text{-trans-syn-down}}$ isomers of $[\text{Fe}^{\text{IV}}(\text{O})(\text{tmc})(\text{OTf})]^+$ and $[\text{Fe}^{\text{IV}}(\text{O})(\text{tmc})]^{2+}$ ions:

The  $[\text{Fe}^{\text{IV}}(\text{O})(\text{tmc})(\text{OTf})]^+$  and  $[\text{Fe}^{\text{IV}}(\text{O})(\text{tmc})]^{2+}$  ions have hydrogen atoms on the propylene and ethylene moieties that face the oxoiron(IV) moiety. Figure 6 shows the free-energy profiles for desaturation of the N-(CH<sub>2</sub>)<sub>3</sub>-N linker for hexa- ( $\mathbf{K}_6$ ) and pentacoordinate ( $\mathbf{K}_5$ ) complexes. Even though we find two close spin states for  $\mathbf{K}_6$ , and a ground-state triplet (lower by 7.8 kcal mol<sup>-1</sup> than  $S=2$ ) for  $\mathbf{K}_5$ , the reaction landscape in both cases is still dominated by the  $S=2$  state reactivity.<sup>[23g,h]</sup> We further found that, as expected from the ‘proximity rule’, the initial hydrogen abstraction is more facile from the N-(CH<sub>2</sub>)<sub>3</sub>-N linker, with respective activation free-energy barriers for  $S=1/S=2$  of 23.9/14.9 kcal mol<sup>-1</sup> in  $^{3,5}\mathbf{K}_6$  and 26.9/20.4 kcal mol<sup>-1</sup> in  $^{3,5}\mathbf{K}_5$ . The corresponding barriers for hydrogen abstraction from the N-(CH<sub>2</sub>)<sub>2</sub>-N linker are 26.4/18.3 for  $^{3,5}\mathbf{K}_6$  and 30.2/23.4 kcal mol<sup>-1</sup> in  $^{3,5}\mathbf{K}_5$  (Tables S14–S16 in the Supporting Information). The loss of water reflects most likely attack of the propylene linker, since oxidation of this linker can also account for the appearance of the  $[M-56]^+$  ion that corresponds to the loss of C<sub>3</sub>H<sub>4</sub>O fragment from the hexacoordinate ion (Table 1). The comparable hydrogen-abstraction barriers for the N-(CH<sub>2</sub>)<sub>2</sub>-N linkers of the  $^{3,5}\mathbf{K}_5$  tmc complex and  $^{3,5}\mathbf{K}_{5\text{-trans-syn-down}}$  of

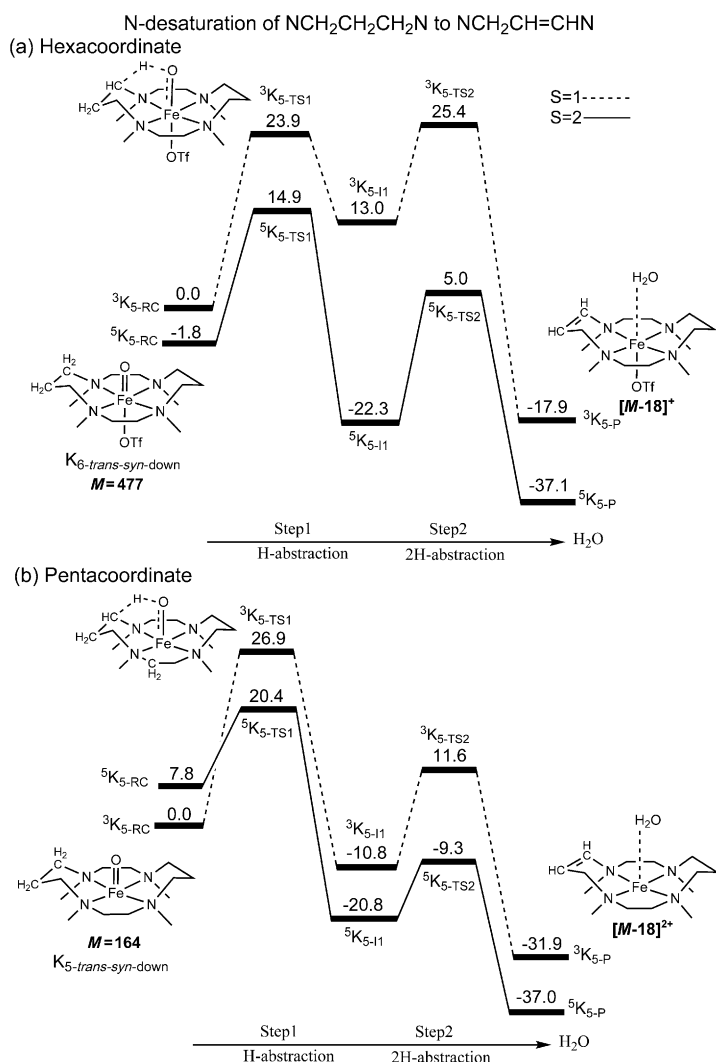


Figure 6. Free-energy profiles [ $\text{kcal mol}^{-1}$ ] at the B2//B1 level of theory for the reactions of a) hexacoordinate  $[\text{Fe}^{\text{IV}}(\text{O})(\text{tmc})(\text{OTf})]^+$ ,  $^3,^5\text{K}_6\text{-trans-syn-down}$  and b) pentacoordinate  $[\text{Fe}^{\text{IV}}(\text{O})(\text{tmc})]^{2+}$  complexes,  $^3,^5\text{K}_5\text{-trans-syn-down}$ . The triplet state of the reactant complex is taken as the reference zero energy.

$[\text{Fe}^{\text{IV}}(\text{O})(\text{bpmen})(\text{OTf})]^+$  ( $29.4/19.5 \text{ kcal mol}^{-1}$ ; Figure 5b) clearly indicate that such a linker in the *trans-syn-down* topology is more favorable for exclusive dehydrogenation pathway.

## Discussion

**Comparison of DFT and experimental results:** Table 2 compares the CID results and the DFT predictions for the various hexa- and pentacoordinate oxoiron(IV) complexes. The table notes the most proximal moieties to the oxoiron(IV) center and the corresponding rate-de-

termining free-energy barriers for activating these moieties on the  $S=2$  surface. The barrier for the DFT-predicted path is labeled by the bold font. The  $S=1$  barriers are invariably higher and are omitted for clarity (see previous section, Figures 4–6, and Figures S3–S5 in the Supporting Information). It can be seen that in most complexes the DFT calculations correctly predict the observed CID peaks. In the case of the pentacoordinate bpmen complex, several isomers were screened, and only the *trans-syn-down* isomer predicts correctly the preferred  $\text{H}_2\text{O}$  loss ( $[\text{M}-18]^{2+}$ ). All other isomers either do not predict the experimental outcome, as found for the *trans-syn-up* isomer, which predicts  $\text{CH}_2\text{O}$  loss ( $[\text{M}-30]^{2+}$ ), or as in the case of the *cis- $\alpha$ -anti* isomer, convert to the *trans-anti* isomer, which predicts  $\text{CH}_2\text{O}$  or PyCHO loss. Considering that DFT predicts correctly all the other cases, we concluded that the observed CID peaks of the pentacoordinate bpmen complex reflect most likely the decay of the *trans-syn-down* isomer. Generally speaking, the observed decay follows the proximity rule and other factors such as steric and strain effects, which contribute to the selectivity among the few available proximal moieties. For example, in the tmc complexes, hydrogen-atom abstraction from the propylene linker is favored over that from the ethylene chain, whereas in the  $\text{L}^8\text{Py}_2$  complexes, the propylene linker is preferentially attacked over the N- $\text{CH}_2$ -Py moieties (Table 2). All in all, these studies emphasize the  $S=2$  state reactivity and the influence of intrinsic factors as the root causes for the regioselectivity towards N-dealkylation versus dehydrogenation, much as found before in intermolecular reactions of synthetic oxoiron(IV) complexes.<sup>[4,6]</sup>

**Electronic structure factors in the intramolecular decay of oxoiron(IV) complexes:** An interesting feature of the intramolecular oxidation reactions of the nonheme oxoiron(IV) complexes we have studied is that, despite the geometric constraints that prevent the  $S=2$  transition state (TS) from assuming its favored upright orientation of the oxidizable C–H bond and the oxoiron(IV) moiety ( $\angle \text{Fe}=\text{O}\cdots\text{HC} \approx 180^\circ$ ),<sup>[17c,23,28]</sup> the lowest energy pathways are still provided by the quintet  $S=2$  state, whereas the triplet  $S=1$  state profiles lie much higher in energy. As is at least shown for the hexacoordinate  $[\text{Fe}^{\text{IV}}(\text{O})(\text{bpmen})(\text{OTf})]^+$  complex (Figure 4), only the  $S=2$  barriers can explain the observed

Table 2. Comparison of CID results and DFT-calculated barriers.

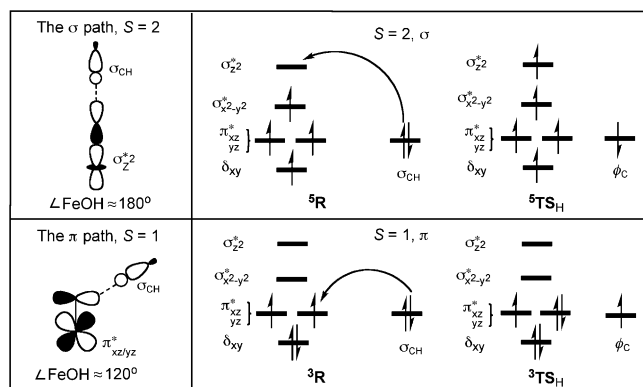
Complex	Most intense CID peak	Topology	Linker in proximity to $\text{Fe}^{\text{IV}}=\text{O}$	Rate determining $\Delta G^*$ for $S=2$ [ $\text{kcal mol}^{-1}$ ]
$[\text{Fe}^{\text{IV}}(\text{O})(\text{L}^8\text{Py}_2)]^{2+}$	$[\text{M}-18]^{2+}$ ( $\text{H}_2\text{O}$ )	<i>trans</i>	N- $\text{CH}_2$ -Py	23.5
			N-( $\text{CH}_2$ ) <sub>3</sub> -N	<b>18.2</b>
$[\text{Fe}^{\text{IV}}(\text{O})(\text{tmc})(\text{OTf})]^+$	$[\text{M}-18]^+$ , $[\text{M}-56]^+$ ( $\text{C}_3\text{H}_4\text{O}$ )	<i>trans-syn-down</i>	N-( $\text{CH}_2$ ) <sub>2</sub> -N	18.3
			N-( $\text{CH}_2$ ) <sub>3</sub> -N	<b>14.9</b>
$[\text{Fe}^{\text{IV}}(\text{O})(\text{tmc})]^{2+}$	$[\text{M}-18]^{2+}$	<i>trans-syn-down</i>	N-( $\text{CH}_2$ ) <sub>2</sub> -N	23.4
			N-( $\text{CH}_2$ ) <sub>3</sub> -N	<b>20.4</b>
$[\text{Fe}^{\text{IV}}(\text{O})(\text{bpmen})(\text{OTf})]^+$	$[\text{M}-30]^+$ ( $\text{CH}_2\text{O}$ )	<i>cis-<math>\alpha</math>-anti</i>	N- $\text{CH}_3$	<b>18.4</b>
			N- $\text{CH}_2$ -Py	19.2
$[\text{Fe}^{\text{IV}}(\text{O})(\text{bpmen})]^{2+}$	$[\text{M}-18]^{2+}$	<i>trans-syn-down</i>	N- $\text{CH}_2$ -Py	23.4
			N-( $\text{CH}_2$ ) <sub>3</sub> -N	<b>19.5</b>

CID decay patterns in a satisfactory manner. We would thus like to understand this spin-state specificity by focusing on the first hydrogen-abstraction step that drives all the mechanisms studied here.

In intermolecular hydrogen-abstraction reactions of oxoiron(IV) reagents, the quintet state has always lower barriers, and it possesses also a distinct TS structure.<sup>[17c,23,28]</sup> In the triplet state, the C–H moiety that undergoes hydrogen abstraction is found to assume a sideways orientation in relation to the oxoiron(IV) moiety, with an Fe–O–HC angle of approximately 120°, whereas in the quintet state, the C–H moiety assumes an upright orientation with an angle close to 180°. These have been termed the  $\pi$  and  $\sigma$  pathways, which correspond to the metal-based orbitals that interact with the C–H moiety as shown in the left panel of Scheme 3.

The origins of these structural features and the enhanced reactivity in the  $S=2$  state have been explained in two different manners. The first explanation relies on the frontier molecular spin–orbital interactions that are available to the two states.<sup>[17c,28a,b,d,e]</sup> It has been argued that the  $\sigma$  pathway is preferred because 1) the  $S=2$  state has more exchange interactions in the d block (four unpaired electrons), thereby resulting in the stabilization of the  $\alpha-\sigma^*_{z^2}$  LUMO orbital of the oxoiron(IV) complex relative to the  $\beta-\pi^*_{xz/yz}$  LUMO; 2)  $\sigma^*_{z^2}$  has a better overlap capability with the  $\sigma_{C-H}$  orbital of the substrate; and 3) there is less steric repulsion between the substrate and the ligand sphere. In contrast, the  $S=1$  state can only proceed along the  $\pi$  pathway and suffers from poorer overlap and higher repulsion of the substrate with the ligand sphere; hence the barrier associated with this pathway is generally higher.

The second approach to the problem<sup>[23]</sup> ascribes both the enhanced reactivity of the  $S=2$  state as well as the two distinct TS orientations to the enhanced exchange reactivity in  $S=2$  versus the reduced number of exchange interactions in the  $S=1$  state. This is illustrated in the electron-shift diagrams in Scheme 3, which show that during hydrogen abstraction in the  $S=2$  state the transferred electron is relegated to the  $\sigma^*_{z^2}$  orbital of the d block of iron and raises the exchange stabilization by the introduction of four new interactions. By contrast, in the  $S=1$  state, the added electron goes to  $\pi^*_{xz}$ , which reduces the exchange stabilization by one interaction. As a result, the  $S=2$  barriers will be small, whereas the  $S=1$  barrier will be considerably larger. Furthermore, the electron-shift diagram predicts that,



Scheme 3. Left panel: The orbital overlap diagrams that predict the  $\pi$  and  $\sigma$  pathways during intermolecular hydrogen-abstraction reactions in the two states. Right panel: Electron-shift diagrams showing the electron reorganization during the establishment of the quintet ( $S=2$ ) and triplet ( $S=1$ ) TS. The total spin of the states refers to the electrons in the d block and in the  $\phi_C$  orbital.

in a given state, the TS will try to assume the geometry that maximizes the overlap between the orbitals that partake in the electron shift, as shown in the overlap diagrams in the left panels in Scheme 3.<sup>[23b]</sup>

In the case of intramolecular reactions as those reported here, the geometric constraints in the complexes prohibit the upright orientation, and both  $S=1$  and  $S=2$  TS are forced to assume an Fe–O–H angle of approximately 100° as shown in Figure 7. Our calculations of the LUMO energies for  $\alpha-\sigma^*_{z^2}$  and  $\beta-\pi^*_{xz}$  show that the orbital energies for  $\alpha-\sigma^*_{z^2}$  and  $\beta-\pi^*_{xz}$  are close and it is not straightforward to decide which of the d orbitals will be more important for the frontier orbital interactions in the TS (Table S5 in the Supporting Information). Previously, it was shown by Solo-

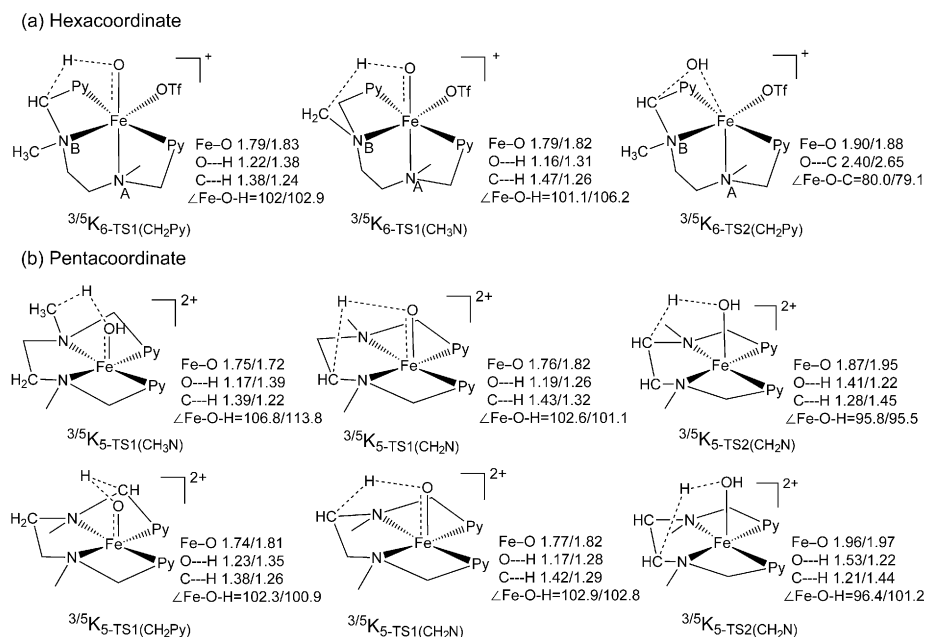


Figure 7. Key geometrical features of  $^{3,5}TS1$  and  $^{3,5}TS2$  of hexacoordinate ( $[Fe^{IV}(O)(bpmen)(OTf)]^+$ ) and pentacoordinate ( $[Fe^{IV}(O)(bpmen)]^{2+}$ ) complexes.

mon et al.<sup>[29]</sup> that for the enzyme HmaS the hydrogen-abstraction TS is constrained and cannot exhibit an upright orientation. The enzyme thus chooses the  $\pi$  pathways on the  $S=2$  state, and the overlap involves the  $\sigma_{\text{CH}}$  with the  $\beta\text{-}\pi^*_{xz/yz}$  LUMO of the oxoiron(IV). It is therefore interesting to discover how the constraints in  $[\text{Fe}^{\text{IV}}(\text{O})(\text{bpmen})\text{(OTf)}]^+$  (**K**<sub>6</sub>) and  $[\text{Fe}^{\text{IV}}(\text{O})(\text{bpmen})]^{2+}$  (**K**<sub>5</sub>) affect the electronic structures of the hydrogen-abstraction TS, and which explanation actually accounts for the observed reactivity.

The d-block orbital energy levels for the hexacoordinate and pentacoordinate oxoiron(IV) complexes of bpmen are quite similar to each other. Furthermore, these orbital diagrams are also similar to the generic diagrams in Scheme 3, and hence we can use the latter scheme as a reference for the following discussion. Figure 8 shows the spin-natural or-

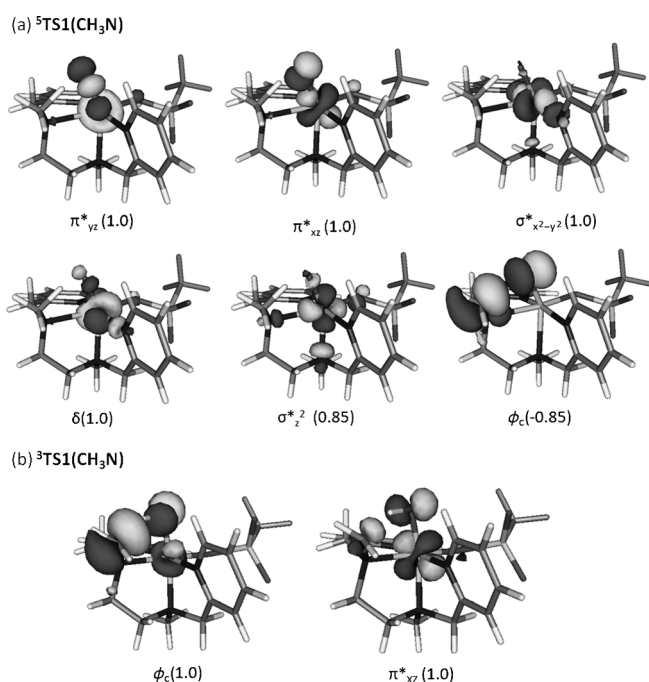


Figure 8. SNOs for the first hydrogen-abstraction TS from the N-CH<sub>3</sub> moiety of the  $[\text{Fe}^{\text{IV}}(\text{O})(\text{bpmen})(\text{OTf})]^+$  complex and their occupation numbers in a)  $^5\text{TS1}(\text{CH}_3\text{N})$  species and b)  $^3\text{TS1}(\text{CH}_3\text{N})$  species.

bitals (SNOs) of the TS for the first hydrogen abstraction from the N-CH<sub>3</sub> group of the  $^3,^5\text{K}_{6\text{-cis-}\alpha\text{-anti}}$  complex. As the SNOs reproduce the spin density of the complex, they are reliable indicators of the electronic structure in DFT. Part (a) shows the SNOs for the quintet  $^5\text{TS1}(\text{CH}_3\text{N})$  species, whereas part (b) displays the SNOs for the corresponding  $^3\text{TS1}(\text{CH}_3\text{N})$  species. Inspection of Figure 8a reveals that the d block of iron contains around 5 electrons with spin  $\alpha$ , including an electron in the  $\sigma^*_{z^2}$  orbital, whereas approximately 1 electron with spin  $\beta$  resides on the CH<sub>2</sub> moiety with some mixture from the oxygen p orbital; hence together we have a quintet-state TS. Even though the SNOs have mixed d character due to the very low symmetry of the TS, the electronic structures of these TS are still virtually the same

as the ones shown in the generic electron-shift diagram in Scheme 3 for the  $S=2$  state. Thus, despite the constraints in the system that prevent an optimal overlap between the  $\sigma_{\text{CH}}$ - and  $\sigma^*_{z^2}$ -type orbitals, the  $^5\text{TS1}(\text{CH}_3\text{N})$  species still contains an electron in the  $\sigma^*_{z^2}$  orbital. This result shows that the driving force for stabilizing the quintet TS is not so much the  $\sigma_{\text{CH}}\text{-}\sigma^*_{z^2}$  overlap, but rather the EER effect due to the increased exchange in the TS.

The hydrogen-abstraction triplet and quintet TS in the pentacoordinate complex behave in a similar manner. Figure 9 shows the SNOs for the hydrogen-abstraction TS form the N-(CH<sub>2</sub>)<sub>2</sub>-N linker. It is seen that, even though the d orbitals undergo intermixing, the  $^3,^5\text{TS1}(\text{CH}_2\text{N})$  species still have SNO sets similar to those for the hexacoordinate complex. The triplet TS has two  $\alpha$ -spin electrons, one in  $\pi^*_{xz}$  and the other in  $\phi_c$  that resides on the N-CH<sub>2</sub> moiety, with admixture from the oxygen p orbital. Thus, once again, despite the constraints that prevent the optimal  $\sigma_{\text{CH}}\text{-}\sigma^*_{z^2}$  overlap, the quintet TS still prefers the electron occupancy that leads to EER and thereby it mediates the entire decay process of both complexes.

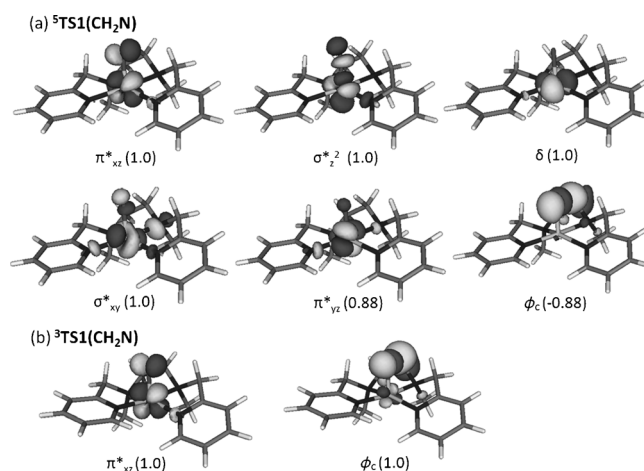


Figure 9. SNOs for the first hydrogen-abstraction TS from the N-CH<sub>2</sub> moiety of the N-(CH<sub>2</sub>)<sub>2</sub>-N linker in  $[\text{Fe}^{\text{IV}}(\text{O})(\text{bpmen})]^{2+}$  and the respective occupation numbers in: a)  $^5\text{TS1}(\text{CH}_2\text{N})$  species and b)  $^3\text{TS1}(\text{CH}_2\text{N})$  species.

## Conclusion

For the first time, experimental and theoretical data for the intramolecular gas-phase reactivity of nonheme oxoiron(IV) species are presented. This work represents a novel technique to understand the intrinsic chemical features of oxoiron(IV) complexes by demonstrating that substrate topology can modulate the reaction landscape. Experimental observations exemplify the complexity of the oxoiron(IV) reaction landscape. On one hand, it is well established that synthetic oxoiron(IV) compounds react in solution with alkanes in a manner similar to monooxygenases.<sup>[30]</sup> In the gas phase, monocationic  $[\text{Fe}^{\text{IV}}(\text{O})(\text{bpmen})(\text{OTf})]^+$  behaves similarly and decays to yield N-dealkylated products, analogous

to the DNA repair iron enzyme *AlkB*.<sup>[31]</sup> On the other hand, dicationic  $[\text{Fe}^{\text{IV}}(\text{O})(\text{bpmen})]^{2+}$  undergoes self-decay to yield a ligand-dehydrogenated product, similar to what is observed in clavaminase synthase and nonheme iron desaturases.<sup>[32]</sup> The variety of reactions carried out by closely related oxoiron(IV) species shows us the effects of substrate nature and proximity on the reactivity of high-valent iron intermediates. It also demonstrates that oxoiron(IV) species are generally indiscriminate about how they react, but that they will oxidize a variety of aliphatic substrates. The principle is rather simple: the chosen mechanism depends on the relative proximity of the various ligand C–H bonds to the oxidant moiety. Even more interesting is the finding that the mechanisms of oxidation in both complex types are generally dominated by the quintet  $S=2$  states, which in the case of the hexacoordinate bpmen also provides the best match to the experimental CID results. This  $S=2$  preference is in line with what is known for bimolecular reactions of oxoiron(IV) complexes, but the present  $S=2$  barriers are larger than those observed for bimolecular reactions. The reason for the latter is the constrained Fe–O–HC angle, which prevents attainment of the ideal upright orientation for maximal overlap of the  $\sigma_{\text{CH}}$  and  $\sigma^*_{\text{z}^2}$  orbitals. Nevertheless, despite the angular constraints on the orbital overlap, the electronic structure of the hydrogen-abstraction quintet transition states involves five d electrons, with one being in the  $\sigma^*_{\text{z}^2}$  orbital, which is in accord with the exchange-enhanced reactivity principle.<sup>[23b,g,h]</sup> EER is thus responsible for the dominance of the  $S=2$  reactions in all the studied complexes.

## Acknowledgements

The work in the L.Q. lab was supported by the U.S. National Institutes of Health (GM-33162) and the U.S. National Science Foundation (CHE1058248). R.M. thanks the Ministerio de Educación y Ciencia of Spain for postdoctoral support. S.S. is supported by the Israel Science Foundation (ISF grant 53/09). S.S. is thankful to Detlef Schröder for useful discussions.

- [1] a) M. Sono, M. P. Roach, E. D. Coulter, J. H. Dawson, *Chem. Rev.* **1996**, *96*, 2841–2887; b) B. Meunier, S. P. de Visser, S. Shaik, *Chem. Rev.* **2004**, *104*, 3947–3980; c) I. G. Denisov, T. M. Makris, S. G. Sligar, I. Schlichting, *Chem. Rev.* **2005**, *105*, 2253–2278.
- [2] a) M. Costas, M. P. Mehn, M. P. Jensen, L. Que Jr., *Chem. Rev.* **2004**, *104*, 939–986; b) R. P. Hausinger, *Crit. Rev. Biochem. Mol. Biol.* **2004**, *39*, 21–68; c) M. M. Abu-Omar, A. Loaiza, N. Hontzas, *Chem. Rev.* **2005**, *105*, 2227–2252; d) C. Krebs, D. Galonić Fujimori, C. T. Walsh, J. M. Bollinger Jr., *Acc. Chem. Res.* **2007**, *40*, 484–492.
- [3] a) J. C. Price, E. W. Barr, T. E. Glass, C. Krebs, J. M. Bollinger Jr., *J. Am. Chem. Soc.* **2003**, *125*, 13008–13009; b) J. C. Price, E. W. Barr, B. Tirupati, J. M. Bollinger Jr., C. Krebs, *Biochemistry* **2003**, *42*, 7497–7508; c) P. J. Riggs-Gelasco, J. C. Price, R. B. Guyer, J. H. Brehm, E. W. Barr, J. M. Bollinger Jr., C. Krebs, *J. Am. Chem. Soc.* **2004**, *126*, 8108–8109; d) J. M. Bollinger Jr., J. C. Price, L. M. Hoffart, E. W. Barr, C. Krebs, *Eur. J. Inorg. Chem.* **2005**, 4245–4254; e) J. C. Price, E. W. Barr, L. M. Hoffart, C. Krebs, J. M. Bollinger Jr., *Biochemistry* **2005**, *44*, 8138–8147; f) L. M. Hoffart, E. W. Barr, R. B. Guyer, J. M. Bollinger Jr., C. Krebs, *Proc. Natl. Acad. Sci. USA* **2006**, *103*, 14738–14743; g) B. E. Eser, E. W. Barr, P. A. Frantom, L. Saleh, J. M. Bollinger, C. Krebs, P. F. Fitzpatrick, *J. Am. Chem. Soc.* **2007**, *129*, 11334–11335; h) D. P. Galonić, E. W. Barr, C. T. Walsh, J. M. Bollinger Jr., C. Krebs, *Nat. Chem. Biol.* **2007**, *3*, 113–116; i) D. Galonić Fujimori, E. W. Barr, M. L. Matthews, G. M. Koch, J. R. Yonce, C. T. Walsh, J. M. Bollinger Jr., C. Krebs, P. J. Riggs-Gelasco, *J. Am. Chem. Soc.* **2007**, *129*, 13408–13409; j) S. Sinnecker, N. Svensen, E. W. Barr, S. Ye, J. M. Bollinger Jr., F. Neese, C. Krebs, *J. Am. Chem. Soc.* **2007**, *129*, 6168–6179.
- [4] a) P. Broun, J. Shanklin, E. Whittle, C. Somerville, *Science* **1998**, *282*, 1315–1317; b) E. J. Whittle, A. E. Tremblay, P. H. Buist, J. Shanklin, *Proc. Natl. Acad. Sci. USA* **2008**, *105*, 14738–14743; c) J. S. Kartha, K. W. Skordos, H. Sun, C. Hall, L. M. Easterwood, C. A. Reilly, E. F. Johnson, G. S. Yost, *Biochemistry* **2008**, *47*, 9756–9770; d) A. Mukherjee, M. Martinho, E. L. Bominaar, E. Münck, L. Que Jr., *Angew. Chem.* **2009**, *121*, 1812–1815; *Angew. Chem. Int. Ed.* **2009**, *48*, 1780–1783; e) D. Usharani, D. Janardanan, S. Shaik, *J. Am. Chem. Soc.* **2011**, *133*, 176–179.
- [5] a) X. Shan, L. Que Jr., *J. Inorg. Biochem.* **2006**, *100*, 421–433; b) L. Que Jr., *Acc. Chem. Res.* **2007**, *40*, 493–500; c) W. Nam, *Acc. Chem. Res.* **2007**, *40*, 522–531.
- [6] a) J.-U. Rohde, J.-H. In, M. H. Lim, W. W. Brennessel, M. R. Bukowski, A. Stubna, E. Münck, W. Nam, L. Que Jr., *Science* **2003**, *299*, 1037–1039; b) M. H. Lim, J.-U. Rohde, A. Stubna, M. R. Bukowski, M. Costas, R. Y. N. Ho, E. Münck, W. Nam, L. Que Jr., *Proc. Natl. Acad. Sci.* **2003**, *100*, 3665–3670; c) M. R. Bukowski, K. D. Koehntop, A. Stubna, E. L. Bominaar, J. A. Halfen, E. Münck, W. Nam, L. Que Jr., *Science* **2005**, *310*, 1000–1002; d) J. Bautz, M. R. Bukowski, M. Kerscher, A. Stubna, P. Comba, A. Lienke, E. Münck, L. Que Jr., *Angew. Chem.* **2006**, *118*, 5810–5813; *Angew. Chem. Int. Ed.* **2006**, *45*, 5681–5684; e) C. V. Sastri, J. Lee, K. Oh, Y. J. Lee, J. Lee, T. A. Jackson, K. Ray, H. Hirao, W. Shin, J. A. Halfen, J. Kim, L. Que Jr., S. Shaik, W. Nam, *Proc. Natl. Acad. Sci. USA* **2007**, *104*, 19181–19186; f) T. A. Jackson, J.-U. Rohde, M. S. Seo, C. V. Sastri, R. DeHont, A. Stubna, T. Ohta, T. Kitagawa, E. Münck, W. Nam, L. Que Jr., *J. Am. Chem. Soc.* **2008**, *130*, 12394–12407; g) Y. Zhou, X. Shan, R. Mas-Ballesté, M. R. Bukowski, A. Stubna, M. Chakrabarti, L. Slominski, J. A. Halfen, E. Münck, L. Que Jr., *Angew. Chem.* **2008**, *120*, 1922–1925; *Angew. Chem. Int. Ed.* **2008**, *47*, 1896–1899; h) M. S. Seo, N. H. Kim, K.-B. Cho, J. E. So, S. K. Park, M. Clemancey, R. Garcia-Serres, J.-M. Latour, S. Shaik, W. Nam, *Chem. Sci.* **2011**, *2*, 1039–1045.
- [7] a) O. Pestovsky, S. Stoian, E. L. Bominaar, X. Shan, E. Münck, L. Que Jr., A. Bakac, *Angew. Chem.* **2005**, *117*, 7031–7034; *Angew. Chem. Int. Ed.* **2005**, *44*, 6871–6874; b) J. England, M. Martinho, E. R. Farquhar, J. R. Frisch, E. L. Bominaar, E. Münck, L. Que Jr., *Angew. Chem.* **2009**, *121*, 3676–3680; *Angew. Chem. Int. Ed.* **2009**, *48*, 3622–3626; c) J. England, Y. Guo, E. R. Farquhar, V. G. Young, Jr., E. Münck, L. Que Jr., *J. Am. Chem. Soc.* **2010**, *132*, 8635–8644; d) D. C. Lacy, R. Gupta, K. L. Stone, J. Greaves, J. W. Ziller, M. P. Hendrich, A. S. Borovik, *J. Am. Chem. Soc.* **2010**, *132*, 12188–12190; e) J. England, Y. Guo, H. K. M. Van, M. A. Cranswick, G. T. Rohde, E. L. Bominaar, E. Münck, L. Que Jr., *J. Am. Chem. Soc.* **2011**, *133*, 11880–11883.
- [8] a) K. Chen, L. Que Jr., *Chem. Commun.* **1999**, 1375–1376; b) R. Mas-Ballesté, M. Costas, T. van den Berg, L. Que Jr., *Chem. Eur. J.* **2006**, *12*, 7489–7500.
- [9] a) P. J. Hay, W. R. Wadt, *J. Chem. Phys.* **1985**, *82*, 299–310; b) C. Lee, W. Yang, R. G. Parr, *Phys. Rev. B* **1988**, *37*, 785; c) A. D. Becke, *J. Chem. Phys.* **1992**, *96*, 2155–2160; d) A. D. Becke, *J. Chem. Phys.* **1992**, *97*, 9173–9177; e) A. D. Becke, *J. Chem. Phys.* **1993**, *98*, 5648–5652; f) R. A. Friesner, R. B. Murphy, M. D. Beachy, M. N. Ringnalda, W. T. Pollard, B. D. Dunietz, Y. Cao, *J. Phys. Chem. A* **1999**, *103*, 1913–1928.
- [10] I. Schrödinger in *Jaguar 7.5*, **2004**.
- [11] Gaussian 03, Revision E.01, M. J. Frisch, G. W. Trucks, H. B. Schlegel, G. E. Scuseria, M. A. Robb, J. R. Cheeseman, J. A. Montgomery, Jr., T. Vreven, K. N. Kudin, J. C. Burant, J. M. Millam, S. S. Iyengar, J. Tomasi, V. Barone, B. Mennucci, M. Cossi, G. Scalmani, N. Rega, G. A. Petersson, H. Nakatsuji, M. Hada, M. Ehara, K. Toyota, R. Fukuda, J. Hasegawa, M. Ishida, T. Nakajima, Y. Honda,

- O. Kitao, H. Nakai, M. Klene, X. Li, J. E. Knox, H. P. Hratchian, J. B. Cross, V. Bakken, C. Adamo, J. Jaramillo, R. Gomperts, R. E. Stratmann, O. Yazyev, A. J. Austin, R. Cammi, C. Pomelli, J. W. Ochterski, P. Y. Ayala, K. Morokuma, G. A. Voth, P. Salvador, J. J. Dannenberg, V. G. Zakrzewski, S. Dapprich, A. D. Daniels, M. C. Strain, O. Farkas, D. K. Malick, A. D. Rabuck, K. Raghavachari, J. B. Foresman, J. V. Ortiz, Q. Cui, A. G. Baboul, S. Clifford, J. Cio-slawski, B. B. Stefanov, G. Liu, A. Liashenko, P. Piskorz, I. Komaromi, R. L. Martin, D. J. Fox, T. Keith, M. A. Al-Laham, C. Y. Peng, A. Nanayakkara, M. Challacombe, P. M. W. Gill, B. Johnson, W. Chen, M. W. Wong, C. Gonzalez, J. A. Pople, Gaussian, Inc., Wallingford CT, **2004**.
- [12] a) H. P. L. S. Portmann, *Chimia* **2000**, *54*, 766–770; b) H. P. L. P. Flückiger, S. Portmann, J. Weber in *Molekul 4.2 2000–2002*.
- [13] S. Grimme, *J. Comput. Chem.* **2006**, *27*, 1787–1799.
- [14] M. Reiher, O. Salomon, B. A. Hess, *Theor. Chim. Acta* **2001**, *107*, 48–55.
- [15] E. A. Duban, K. P. Bryliakov, E. P. Talsi, *Eur. J. Inorg. Chem.* **2007**, 852–857.
- [16] O. V. Makhlynets, E. V. Rybak-Akimova, *Chem. Eur. J.* **2010**, *16*, 13995–14006.
- [17] a) A. Decker, J.-U. Rohde, L. Que, Jr., E. I. Solomon, *J. Am. Chem. Soc.* **2004**, *126*, 5378–5379; b) A. Decker, M. D. Clay, E. I. Solomon, *J. Inorg. Biochem.* **2006**, *100*, 697–706; c) A. Decker, J.-U. Rohde, E. J. Klinker, S. D. Wong, L. Que, Jr., E. I. Solomon, *J. Am. Chem. Soc.* **2007**, *129*, 15983–15996.
- [18] D. Agrawal, D. Schröder, *Organometallics* **2011**, *30*, 32–35.
- [19] P. Chen, *Angew. Chem.* **2003**, *115*, 2938–2954; *Angew. Chem. Int. Ed.* **2003**, *42*, 2832–2847.
- [20] W. A. Donald, C. J. McKenzie, R. A. J. O'Hair, *Angew. Chem. Int. Ed.* **2011**, *50*, 8379–8383.
- [21] a) P. Mialane, L. Tchertanova, F. Banse, J. Sainton, J.-J. Girerd, *Inorg. Chem.* **2000**, *39*, 2440–2444; b) N. Raffard, V. Balland, J. Simaan, S. Létard, M. Nierlich, K. Miki, F. Banse, E. Anxolabéhère-Mallarta, J.-J. Girerd, *C. R. Chim.* **2002**, *5*, 99–109; c) M. Costas, L. Que, Jr., *Angew. Chem.* **2002**, *114*, 2283–2285; *Angew. Chem. Int. Ed.* **2002**, *41*, 2179–2181; d) S. Taktak, M. Flook, B. M. Foxman, L. Que, Jr., E. V. Rybak-Akimova, *Chem. Commun.* **2005**, 5301–5303; e) R. Mas-Ballesté, L. Que, Jr., *J. Am. Chem. Soc.* **2007**, *129*, 15964–15972; f) M. S. Chen, M. C. White, *Science* **2007**, *318*, 783–787.
- [22] a) Y. Wang, D. Kumar, C. Yang, K. Han, S. Shaik, *J. Phys. Chem. B* **2007**, *111*, 7700–7710; b) D. Li, Y. Wang, C. Yang, K. Han, *Dalton Trans.* **2009**, 291–297.
- [23] a) For the first mention of exchange enhancements, see: D. Kumar, H. Hirao, L. Que, Jr., S. Shaik, *J. Am. Chem. Soc.* **2005**, *127*, 8026–8027; b) H. Hirao, D. Kumar, W. Thiel, S. Shaik, *J. Am. Chem. Soc.* **2005**, *127*, 13007–13018; c) H. Hirao, D. Kumar, L. Que, Jr., S. Shaik, *J. Am. Chem. Soc.* **2006**, *128*, 8590–8606; d) S. P. de Visser, *J. Am. Chem. Soc.* **2006**, *128*, 9813–9824; e) S. Shaik, H. Hirao, D. Kumar, *Acc. Chem. Res.* **2007**, *40*, 532–542; f) E. J. Klinker, S. Shaik, H. Hirao, L. Que Jr., *Angew. Chem.* **2009**, *121*, 1317–1321; *Angew. Chem. Int. Ed.* **2009**, *48*, 1291–1295; g) D. Janardanan, Y. Wang, P. Schyman, L. Que, Jr., S. Shaik, *Angew. Chem.* **2010**, *122*, 3414–3417; *Angew. Chem. Int. Ed.* **2010**, *49*, 3342–3346; h) S. Shaik, H. Chen, D. Janardanan, *Nat. Chem.* **2011**, *3*, 19–27.
- [24] a) K. Nehru, M. S. Seo, J. Kim, W. Nam, *Inorg. Chem.* **2007**, *46*, 293–298; b) B. Chiavarino, R. Cipollini, M. E. Crestoni, S. Fornarini, F. Lanucara, A. Lapi, *J. Am. Chem. Soc.* **2008**, *130*, 3208–3217.
- [25] a) J. F. Hull, D. Balcells, E. L. O. Sauer, C. Raynaud, G. W. Brudvig, R. H. Crabtree, O. Eisenstein, *J. Am. Chem. Soc.* **2010**, *132*, 7605–7616; b) M. A. Bigi, S. A. Reed, M. C. White, *Nat. Chem.* **2011**, *3*, 216–222.
- [26] M. Schlängen, J. Neugebauer, M. Reiher, D. Schröder, J. P. López, M. Haryono, F. W. Heinemann, A. Grohmann, H. Schwarz, *J. Am. Chem. Soc.* **2008**, *130*, 4285–4294.
- [27] D. Schröder, M. C. Holthausen, H. Schwarz, *J. Phys. Chem. B* **2004**, *108*, 14407–14416.
- [28] a) L. Bernasconi, M. J. Louwerse, E. J. Baerends, *Eur. J. Inorg. Chem.* **2007**, 3023–3033; b) M. J. Louwerse, E. J. Baerends, *Phys. Chem. Chem. Phys.* **2007**, *9*, 156–166; c) A. J. Johansson, M. R. A. Blomberg, P. E. M. Siegbahn, *J. Phys. Chem. C* **2007**, *111*, 12397–12406; d) C. Michel, E. J. Baerends, *Inorg. Chem.* **2009**, *48*, 3628–3638; e) E. I. Solomon, S. D. Wong, L. V. Liu, A. Decker, M. S. Chow, *Curr. Opin. Chem. Biol.* **2009**, *13*, 99–113; f) C. Geng, S. Ye, F. Neese, *Angew. Chem.* **2010**, *122*, 5853–5856; *Angew. Chem. Int. Ed.* **2010**, *49*, 5717–5720; g) S. Ye, F. Neese, *Proc. Natl. Acad. Sci. USA* **2011**, *108*, 1228–1233.
- [29] M. L. Neidig, A. Decker, O. W. Choroba, F. Huang, M. Kavana, G. R. Moran, J. B. Spencer, E. I. Solomon, *Proc. Natl. Acad. Sci. USA* **2006**, *103*, 12966–12973.
- [30] J. Kaizer, E. J. Klinker, N. Y. Oh, J.-U. Rohde, W. J. Song, A. Stubna, J. Kim, E. Münck, W. Nam, L. Que Jr., *J. Am. Chem. Soc.* **2004**, *126*, 472–473.
- [31] P. Ø. Farnes, R. F. Johansen, E. Seeberg, *Nature* **2002**, *419*, 178–182.
- [32] B. G. Fox, K. S. Lyle, C. E. Rogge, *Acc. Chem. Res.* **2004**, *37*, 421–429.

Received: January 10, 2012

Revised: March 16, 2012

Published online: July 26, 2012